The first 7 months of the 2020 X-ray outburst of the magnetar SGR J1935+2154

A. Borghese[1,2]★, F. Coti Zelati[1,2], G.L. Israel[3], M. Pilia[4], M. Burgay[4], M. Trudu[4], S. Zane[5], R. Turolla[5,6], N. Rea[1,2], P. Esposito[7,8], S. Mereghetti[8], A. Tiengo[7,8,9], A. Possenti[4,10]

[1]*Institute of Space Sciences (ICE, CSIC), Campus UAB, Carrer de Can Magrans s/n, E-08193, Barcelona, Spain*
[2]*Institut d'Estudis Espacials de Catalunya (IEEC), Carrer Gran Capità 2–4, E-08034 Barcelona, Spain*
[3]*INAF–Osservatorio Astronomico di Roma, via Frascati 33, 00078 Monteporzio Catone, Italy*
[4]*INAF–Osservatorio Astronomico di Cagliari, Via della Scienza 5, I-09047 Selargius, Italy*
[5]*Mullard Space Science Laboratory, University College London, Holmbury St. Mary, Dorking, Surrey RH5 6NT, UK*
[6]*Dipartimento di Fisica e Astronomia Galileo Galilei, Universitá di Padova, via F. Marzolo 8, I-35131 Padova, Italy*
[7]*Scuola Universitaria Superiore IUSS Pavia, Palazzo del Broletto, piazza della Vittoria 15, I-27100 Pavia, Italy*
[8]*INAF–Istituto di Astrofisica Spaziale e Fisica Cosmica di Milano, via A. Corti 12, I-20133 Milano, Italy*
[9]*Istituto Nazionale di Fisica Nucleare (INFN), Sezione di Pavia, via A. Bassi 6, I-27100 Pavia, Italy*
[10]*Department of Physics, Università di Cagliari, S.P. Monserrato-Sestu km 0,700, I-09042 Monserrato, Italy*

Accepted XXX. Received YYY; in original form ZZZ

ABSTRACT

The magnetar SGR J1935+2154 underwent a new active episode on 2020 April 27–28, when a forest of hundreds of X-ray bursts and a large enhancement of the persistent flux were detected. For the first time, a radio burst with properties similar to those of fast radio bursts and with a X-ray counterpart was observed from this source, showing that magnetars can power at least a group of fast radio bursts. In this paper, we report on the X-ray spectral and timing properties of SGR J1935+2154 based on a long-term monitoring campaign with *Chandra*, *XMM–Newton*, *NuSTAR*, *Swift* and *NICER* covering a time span of ~ 7 months since the outburst onset. The broadband spectrum exhibited a non-thermal power-law component ($\Gamma \sim 1.2$) extending up to $\sim 20-25$ keV throughout the campaign and a blackbody component with temperature decreasing from ~ 1.5 keV at the outburst peak to ~ 0.45 keV in the following months. We found that the luminosity decay is well described by the sum of two exponential functions, reflecting the fast decay (~1 d) at the early stage of the outburst followed by a slower decrease (~30 d). The source reached quiescence about ~ 80 days after the outburst onset, releasing an energy of $\sim 6\times10^{40}$ erg during the outburst. We detected X-ray pulsations in the *XMM–Newton* data sets and derived an average spin-down rate of $\sim 3.5\times10^{-11}$ s s^{-1} using the spin period measurements derived in this work and three values reported previously during the same active period. Moreover, we report on simultaneous radio observations performed with the Sardinia Radio Telescope. No evidence for periodic or single-pulse radio emission was found.

Key words: Magnetars; Neutron stars; Radio pulsars; Transient sources; X-ray bursts

1 INTRODUCTION

Among isolated neutron stars, magnetars are the most active, with a distinctive high-energy phenomenology (see, e.g., Kaspi & Beloborodov 2017; Esposito et al. 2021, for recent reviews). Powered by their own magnetic energy, which is stored in a superstrong field (up to ~10^{15} G at the surface), these objects emit X-ray/gamma-ray bursts that last from milliseconds to tens of minutes and reach a wide range of X-ray peak luminosities, $10^{39}-10^{45}$ erg s^{-1}. These flaring events are often accompanied by long-lived (up to years) enhancements of the persistent X-ray luminosity, the so-called outbursts (see http://magnetars.ice.csic.es; Coti Zelati et al. 2018).

Discovered in 2014 (Stamatikos et al. 2014), SGR J1935+2154 (henceforth SGR J1935) has a spin period $P \sim 3.25$ s and a spin-down rate $\dot{P} \sim 1.4\times10^{-11}$ s s^{-1}, implying a surface dipolar magnetic field $B_{\rm p} \sim 2.2\times10^{14}$ G at the pole (Israel et al. 2016). Since its discovery, SGR J1935 has been one of the most active magnetars, showing outbursts in 2015 February, 2016 May and June, and frequent bursting episodes (see, e.g., Younes et al. 2017; Lin et al. 2020b). Its latest reactivation dates back to 2020 April 27, when several X-ray and gamma-ray instruments detected a burst storm and an increase of the persistent X-ray flux (e.g., Palmer 2020; Younes et al. 2020). A day after the initial trigger, the Canadian Hydrogen Intensity Mapping Experiment (CHIME) and the Survey for Transient Astronomical Radio Emission 2 (STARE2) independently detected an extremely bright radio burst (Andersen et al. 2020; Bochenek et al. 2020), with morphology reminiscent of that of Fast Radio Bursts (FRBs; see, e.g., Caleb & Keane 2021, for a review). The energy released was about

★ E-mail: borghese@ice.csic.es

ORIGINAL UNEDITED MANUSCRIPT

Downloaded from https://academic.oup.com/mnras/advance-article/doi/10.1093/mnras/stac1314/6584863 by UCL Library Services user on 16 May 2022

© 2022 The Author(s) Published by Oxford University Press on behalf of Royal Astronomical Society

three orders of magnitude larger than that of any radio pulse from the Crab pulsar (the source emitting the brightest Galactic radio pulses; Bera & Chengalur 2019) and any giant pulse detected from the radio magnetar XTE J1810–197 (Caleb et al. 2022), and ∼50 times smaller than that released by the weakest extragalactic FRB observed so far (e.g., Marcote et al. 2020). This detection strengthened the hypothesis that at least a sub-group of FRBs can be powered by magnetars at cosmological distances (Beloborodov 2017; Margalit et al. 2020). Moreover, the radio burst was temporally coincident with a hard X-ray burst (Mereghetti et al. 2020; Tavani et al. 2021; Ridnaia et al. 2021), showing for the first time that magnetar bursts can have a bright radio counterpart. Furthermore, analysis of simultaneous radio and X-ray archival observations of magnetars revealed two FRB-like bursts from another source, 1E 1547.0–5408 (Israel et al. 2021). One of the radio bursts was anticipated by ∼1 s by a short X-ray burst, resulting in a radio-to-X-ray fluence ratio of $\sim 10^{-9}$, proving that magnetars can emit radio bursts with fluences spanning over a wide range.

No pulsed radio emission from SGR J1935 was detected in the immediate aftermath of the FRB-like event (Lin et al. 2020a). Coordinated radio and X-ray monitoring campaigns were initiated. While no other simultaneous radio and X-ray bursts were observed, SGR J1935 emitted a few more fainter radio bursts (Kirsten et al. 2020; Zhang et al. 2020) and several X-ray short bursts (see `http://enghxmt.ihep.ac.cn/bfy/331.jhtml` and Table 2 by Borghese et al. 2020). On 2020 October 8, CHIME detected three additional radio bursts from the direction of SGR J1935, all clustered within one rotational period cycle (Good & Chime/Frb Collaboration 2020). Follow-up observations with the Five-hundred-metre Aperture Sperical Telescope (FAST) caught numerous single pulses from the source and also detected pulsed radio emission (Zhu et al. 2020). These detections indicated that SGR J1935 can emit radio bursts with energies spanning nearly seven orders of magnitude and switch on/off in the radio band.

Here, we report on the results of the X-ray long-term monitoring campaign of SGR J1935 covering the first ∼7 months of the outburst decay since its reactivation on 2020 April 27. We first summarise the data analysis procedure in Section 2. We then present the timing and spectral analysis, as well as a search for short bursts in Section 3. Simultaneous radio observations are described in Section 4. Finally, we discuss our findings in Section 5.

ORIGINAL UNEDITED MANUSCRIPT

Downloaded from https://academic.oup.com/mnras/advance-article/doi/10.1093/mnras/stac1314/6584863 by UCL Library Services user on 16 May 2022

Table 1. Log of the X-ray and radio observations of SGR J1935 analysed in this work.

X-ray Instrument[a]	Obs.ID	Start YYYY-MM-DD hh:mm:ss (TT)	Stop	Exposure (ks)	Count Rate[b] (counts s^{-1})	kT_{BB} (keV)	R_{BB} (km)	Flux[c] (10^{-12} cgs)
Chandra/ACIS (TE)	22431	2020-04-30 20:30:28	2020-05-01 02:44:51	19.8	0.147±0.003	0.51±0.03	2.1±0.2	4.6±0.4
Chandra/ACIS (TE)	22432	2020-05-02 08:58:14	2020-05-02 23:29:51	49.9	0.137±0.002	0.56±0.01	1.34±0.05	4.0±0.1
XMM–Newton/EPIC-pn (FF)	0871190201	2020-05-13 21:43:24	2020-05-14 10:54:26	28.3	0.388±0.004	0.45±0.01	1.7±0.1	2.5±0.1
Chandra/ACIS (TE)	23251	2020-05-18 10:48:14	2020-05-18 16:32:19	18.8	0.116±0.002	0.50±0.01	1.5±0.1	3.0±0.1
NICER/XTI	3655010201	2020-05-18 05:36:06	2020-05-18 13:38:40	4.7	0.29±0.01	0.49±0.02	1.3±0.2	0.9±0.1
NICER/XTI	3020560105[d1]	2020-05-19 21:53:47	2020-05-19 22:10:40	0.9	0.50±0.03	$0.51^{+0.01}_{-0.03}$	1.5±0.2	1.7±0.1
NICER/XTI	3020560106[d1]	2020-05-20 07:39:40	2020-05-20 15:37:20	0.6	0.67±0.04	$0.51^{+0.01}_{-0.03}$	1.5±0.2	1.7±0.1
NICER/XTI	3020560107	2020-05-22 00:59:19	2020-05-22 22:54:46	5.1	0.49±0.01	0.47±0.02	1.5±0.1	2.1±0.1
NICER/XTI	3020560108	2020-05-23 00:13:19	2020-05-23 09:42:50	3.2	0.39±0.02	0.45±0.02	1.8±0.2	1.0±0.1
NICER/XTI	3020560109[d2]	2020-05-25 14:13:00	2020-05-25 15:55:32	0.8	0.53±0.03	0.44±0.02	1.8±0.1	1.8±0.1
Swift/XRT (PC)	00033349067	2020-05-28 12:10:39	2020-05-28 16:59:54	2.0	0.024±0.004	$0.37^{+0.09}_{-0.07}$	$1.8^{+2.0}_{-0.6}$	$1.9^{+0.4}_{-0.3}$
NICER/XTI	3020560110[d2]	2020-05-28 21:10:39	2020-05-28 23:00:55	1.7	0.43±0.02	0.44±0.02	1.8±0.1	1.8±0.1
NICER/XTI	3020560111[d3]	2020-05-29 03:22:38	2020-05-29 03:39:46	0.9	0.38±0.03	0.48±0.04	1.5±0.02	1.7±0.1
NICER/XTI	3020560112[d3]	2020-05-30 05:42:03	2020-05-30 18:18:57	1.3	0.49±0.03	0.48±0.04	1.5±0.02	1.7±0.1
NICER/XTI	3020560113[d4]	2020-05-31 01:50:42	2020-05-31 11:24:40	1.1	0.49±0.03	0.43±0.02	1.6±0.02	2.6±0.2
NICER/XTI	3020560114[d4]	2020-06-01 02:37:42	2020-06-01 21:50:40	2.7	0.43±0.02	0.43±0.02	1.6±0.02	2.6±0.2
NICER/XTI	3020560115[d4]	2020-06-02 23:34:38	2020-06-02 23:51:40	1.0	0.47±0.03	0.43±0.02	1.6±0.02	2.6±0.2
NICER/XTI	3020560116[d5]	2020-06-03 04:12:40	2020-06-03 04:25:13	0.7	0.41±0.04	0.50±0.02	1.2±0.1	0.9±0.1
NICER/XTI	3020560117[d5]	2020-06-04 12:45:40	2020-06-04 13:10:23	1.4	0.37±0.02	0.50±0.02	1.2±0.1	0.9±0.1
Swift/XRT (PC)	00033349068	2020-06-05 03:37:29	2020-06-05 09:53:53	1.5	0.021±0.004	$0.4^{+0.2}_{-0.1}$	$1.6^{+5.7}_{-0.7}$	$2.6^{+0.8}_{-0.7}$
NICER/XTI	3020560118[d5]	2020-06-05 04:14:56	2020-06-05 16:59:23	1.2	0.30±0.02	0.50±0.02	1.2±0.1	0.9±0.1
NICER/XTI	3020560119[d5]	2020-06-06 05:03:57	2020-06-06T05:22:00	1.0	0.20±0.02	0.50±0.02	1.2±0.1	0.9±0.1
Swift/XRT (PC)	00033349069	2020-06-11 01:14:49	2020-06-11 14:16:52	2.5	0.023±0.003	$0.55^{+0.10}_{-0.09}$	$0.9^{+0.4}_{-0.2}$	2.9±0.4
NuSTAR FPMA/B	80602313006[e]	2020-06-14 06:46:09	2020-06-14 23:21:09	30.1/29.4	0.073±0.002	0.44±0.04	$2.0^{+1.0}_{-0.5}$	2.0±0.1
Swift/XRT (PC)	00089040001[e]	2020-06-14 10:25:15	2020-06-1413:49:53	1.9	0.029±0.004	0.44±0.04	$2.0^{+1.0}_{-0.5}$	2.0±0.1
NICER/XTI	3655010301[d6]	2020-06-17 21:38:39	2020-06-17 22:06:40	1.2	0.33±0.03	0.46±0.01	1.4±0.1	1.4±0.1
Swift/XRT (PC)	00033349070	2020-06-18 08:23:18	2020-06-18 23:11:53	2.7	0.029±0.003	$0.50^{+0.06}_{-0.05}$	$1.4^{+0.4}_{-0.3}$	1.4±0.2
NICER/XTI	3655010302[d6]	2020-06-18 08:29:43	2020-06-18 21:21:20	6.6	0.38±0.01	0.46±0.01	1.4±0.1	1.4±0.1
NICER/XTI	3655010303[d6]	2020-06-18 23:59:32	2020-06-19 09:45:00	4.1	0.21±0.01	0.46±0.01	1.4±0.1	1.4±0.1
NICER/XTI	3020560120[d7]	2020-06-20 21:05:40	2020-06-20 21:23:40	0.9	0.46±0.03	0.42±0.01	1.8±0.2	1.7±0.1
NICER/XTI	3020560121[d7]	2020-06-21 00:01:20	2020-06-21 00:29:20	0.8	0.31±0.03	0.42±0.01	1.8±0.2	1.7±0.1
NICER/XTI	3020560122[d7]	2020-06-22 10:17:00	2020-06-22 10:49:20	1.7	0.41±0.02	0.42±0.01	1.8±0.2	1.7±0.1
NICER/XTI	3020560123	2020-06-23 01:36:00	2020-06-23 17:48:20	3.2	0.31±0.01	0.45±0.01	1.5±0.1	0.8±0.1
NICER/XTI	3020560124[d8]	2020-06-24 22:41:19	2020-06-24 23:13:11	1.8	0.35±0.02	0.47±0.02	1.5±0.01	1.0±0.1
Swift/XRT (PC)	00033349071	2020-06-25 01:30:52	2020-06-25 17:43:52	3.2	0.025±0.003	0.38±0.06	$1.9^{+1.2}_{-0.5}$	$1.6^{+0.4}_{-0.3}$
NICER/XTI	3020560125[d8]	2020-06-25 21:57:00	2020-06-25 22:29:00	1.6	0.37±0.03	0.47±0.02	1.5±0.01	1.0±0.1

[a] The instrumental setup is indicated in brackets: TE = timed exposure, FF = full frame, PC = photon counting, WT = windowed timing.

[b] Count rate, computed after removing bursts, in the 0.3–10 keV range for *Swift* and *XMM–Newton*, in the 0.3–8 keV interval for *Chandra*, in the 1–5 keV band for *NICER*, and in the 3–20 keV range for *NuSTAR* summing up the two FPMs. Uncertainties are at 1σ c.l.

[c] Observed 0.3–10 keV flux in units of 10^{-12} erg cm^{-2} s^{-1}.

[d,e,f] The spectra extracted from these observations were fitted jointly, tying up all model parameters (see Section 3.2.1 for details).

ORIGINAL UNEDITED MANUSCRIPT

Downloaded from https://academic.oup.com/mnras/advance-article/doi/10.1093/mnras/stac1314/6584863 by UCL Library Services user on 16 May 2022

Downloaded from https://academic.oup.com/mnras/advance-article/doi/10.1093/mnras/stac1314/6584863 by UCL Library Services user on 16 May 2022

Table 1 – *continued*

X-ray Instrument[a]	Obs.ID	Start YYYY-MM-DD hh:mm:ss (TT)	Stop YYYY-MM-DD hh:mm:ss (TT)	Exposure (ks)	Count Rate[b] (counts s^{-1})	kT_{BB} (keV)	R_{BB} (km)	Flux[c] (10^{-12} cgs)
NICER/XTI	3020560126[d9]	2020-06-27 14:29:00	2020-06-27 14:45:20	0.8	0.38±0.03	0.45±0.03	1.5±0.2	1.1±0.1
NICER/XTI	3020560127[d9]	2020-06-28 16:31:00	2020-06-28 17:04:51	1.7	0.29±0.02	0.45±0.03	1.5±0.2	1.1±0.1
NICER/XTI	3020560128[d9]	2020-06-29 18:53:20	2020-06-29 19:24:40	1.7	0.31±0.02	0.45±0.03	1.5±0.2	1.1±0.1
NICER/XTI	3020560129[d10]	2020-06-30 16:19:20	2020-06-30 17:03:20	2.1	0.29±0.02	0.46±0.01	1.5±0.1	0.9±0.1
NICER/XTI	3020560130[d10]	2020-07-01 12:25:57	2020-07-01 12:40:50	0.6	0.41±0.04	0.46±0.01	1.5±0.1	0.9±0.1
NICER/XTI	3020560131[d10]	2020-07-02 11:41:29	2020-07-02 12:03:20	1.2	0.27±0.02	0.46±0.01	1.5±0.1	0.9±0.1
Swift/XRT (PC)	00033349072	2020-07-02 16:24:24	2020-07-02 18:27:52	3.2	0.026±0.003	$0.51^{+0.08}_{-0.07}$	$1.2^{+0.5}_{-0.2}$	3.4±0.4
NICER/XTI	3020560132[d10]	2020-07-03 14:01:00	2020-07-03 14:22:40	1.1	0.37±0.02	0.46±0.01	1.5±0.1	0.9±0.1
NICER/XTI	3020560133[d10]	2020-07-04 19:30:37	2020-07-04 19:47:06	0.8	0.33±0.03	0.46±0.01	1.5±0.1	0.9±0.1
NICER/XTI	3020560134[d11]	2020-07-08 18:21:40	2020-07-08 18:32:57	0.5	0.31±0.05	0.43±0.02	1.6±0.2	0.7±0.1
Swift/XRT (PC)	00033349073	2020-07-09 11:17:01	2020-07-09 21:01:52	3.4	0.027±0.003	0.44±0.05	$1.6^{+0.5}_{-0.3}$	1.4±0.2
NICER/XTI	3020560135[d11]	2020-07-10 05:43:00	2020-07-10 05:50:07	0.4	0.28±0.04	0.43±0.02	1.6±0.2	0.7±0.1
NICER/XTI	3020560136[d11]	2020-07-11 10:02:40	2020-07-11 11:47:40	1.3	0.26±0.03	0.43±0.02	1.6±0.2	0.7±0.1
NICER/XTI	3020560137[d11]	2020-07-12 20:07:20	2020-07-12 20:19:40	0.7	0.31±0.03	0.43±0.02	1.6±0.2	0.7±0.1
NICER/XTI	3020560138[d12]	2020-07-15 16:02:00	2020-07-15 19:35:40	3.1	0.23±0.02	0.42±0.01	1.8±0.1	0.7±0.1
NICER/XTI	3020560139[d12]	2020-07-16 06:07:56	2020-07-16 17:17:00	1.4	0.32±0.02	0.42±0.01	1.8±0.1	0.7±0.1
Swift/XRT (PC)	00033349074	2020-07-16 12:20:27	2020-07-16 23:36:52	1.5	0.026±0.004	$0.55^{+0.10}_{-0.09}$	$1.0^{+0.5}_{-0.2}$	1.2±0.2
NICER/XTI	3020560140[d12]	2020-07-17 03:22:40	2020-07-17 03:40:40	0.9	0.12±0.03	0.42±0.01	1.8±0.1	0.7±0.1
NICER/XTI	3020560141[d12]	2020-07-19 00:23:40	2020-07-19 00:40:20	0.8	0.33±0.03	0.42±0.01	1.8±0.1	0.7±0.1
Swift/XRT (PC)	00033349075	2020-07-21 22:49:04	2020-07-21 23:02:54	0.8	0.034±0.006	0.4±0.1	$1.5^{+2.4}_{-0.6}$	1.1±0.3
Swift/XRT (WT)	00033349076	2020-07-24 00:01:53	2020-07-24 01:46:56	2.9	0.02±0.01	–	–	–
Swift/XRT (PC)	00033349077	2020-07-30 04:17:06	2020-07-30 20:35:54	2.4	0.024±0.003	$0.53^{+0.07}_{-0.08}$	$1.1^{+0.5}_{-0.2}$	2.4±0.6
NICER/XTI	3020560143[d13]	2020-07-31 19:03:58	2020-07-31 20:50:03	1.3	0.33±0.02	0.43±0.03	$1.7^{+0.3}_{-0.1}$	1.2±0.3
NICER/XTI	3020560144[d13]	2020-08-01 16:45:40	2020-08-01 17:12:36	1.4	0.32±0.02	0.43±0.03	$1.7^{+0.3}_{-0.1}$	1.2±0.3
NICER/XTI	3020560146[d14]	2020-08-03 09:22:40	2020-08-03 18:48:54	1.9	0.52±0.02	0.39±0.03	$1.7^{+0.3}_{-0.2}$	3.3±0.3
Swift/XRT (PC)	00033349078	2020-08-04 01:59:14	2020-08-04 02:07:53	0.5	0.013±0.005	$0.7^{+0.5}_{-0.2}$	$0.5^{+0.6}_{-0.2}$	$6.9^{+31.4}_{-6.7}$
NICER/XTI	3020560147[d14]	2020-08-04 20:40:00	2020-08-04 21:07:36	0.8	0.34±0.03	0.39±0.03	$1.7^{+0.3}_{-0.2}$	3.3±0.3
Swift/XRT (PC)	00033349079	2020-08-06 06:40:52	2020-08-06 23:07:52	2.9	0.015±0.002	$0.26^{+0.08}_{-0.05}$	$4.8^{+8.7}_{-1.9}$	$0.8^{+0.2}_{-0.1}$
NICER/XTI	3020560148[d14]	2020-08-06 12:56:23	2020-08-06 16:27:29	2.2	0.37±0.02	0.39±0.03	$1.7^{+0.3}_{-0.2}$	3.3±0.3
Swift/XRT (PC)	00033349080	2020-08-13 18:54:37	2020-08-13 19:07:52	0.8	0.020±0.005	0.5±0.2	$1.2^{+2.5}_{-0.4}$	$2.3^{+1.2}_{-1.1}$
Swift/XRT (PC)	00033349081	2020-08-15 20:17:15	2020-08-15 23:51:54	2.4	0.027±0.003	0.44±0.07	$1.6^{+1.0}_{-0.4}$	2.2±0.6
Swift/XRT (PC)	00033349082	2020-08-25 17:37:39	2020-08-25 19:35:53	2.9	0.021±0.003	$0.40^{+0.07}_{-0.06}$	$1.7^{+1.0}_{-0.4}$	$1.3^{+0.3}_{-0.2}$
NICER/XTI	3020560149[d15]	2020-08-28 21:22:25	2020-08-28 21:41:20	0.3	0.54±0.06	0.44±0.04	1.6±0.2	1.4±0.5
Swift/XRT (PC)	00033349083	2020-09-05 00:49:21	2020-09-05 05:33:54	2.0	0.027±0.003	$0.43^{+0.05}_{-0.04}$	$1.7^{+0.6}_{-0.3}$	1.4±0.2
Swift/XRT (WT)	00033349084	2020-09-10 22:39:20	2020-09-10 23:59:56	1.5	0.05±0.01	–	–	–
NICER/XTI	3020560151[d15]	2020-09-11 05:55:00	2020-09-11 07:51:00	2.1	0.32±0.02	0.44±0.04	1.6±0.2	1.4±0.5
Swift/XRT (WT)	00033349085	2020-09-11 09:43:06	2020-09-11 11:15:56	2.2	0.034±0.008	–	–	–
Swift/XRT (WT)	00033349086	2020-09-17 16:52:17	2020-09-17 23:20:56	3.3	0.049±0.006	–	–	–
Swift/XRT (WT)	00033349087	2020-09-18 00:50:43	2020-09-18 02:34:56	1.7	0.039±0.008	–	–	–

[a] The instrumental setup is indicated in brackets: TE = timed exposure, FF = full frame, PC = photon counting, WT = windowed timing.

[b] Count rate, computed after removing bursts, in the 0.3–10 keV range for *Swift* and *XMM–Newton*, in the 0.3–8 keV interval for *Chandra*, in the 1–5 keV band for *NICER*, and in the 3–20 keV range for *NuSTAR* summing up the two FPMs. Uncertainties are at 1σ c.l.

[c] Observed 0.3–10 keV flux in units of 10^{-12} erg cm^{-2} s^{-1}.

[d,e,f] The spectra extracted from these observations were fitted jointly, tying up all model parameters (see Section 3.2.1 for details).

ORIGINAL UNEDITED MANUSCRIPT

Table 1 – *continued*

X-ray Instrument[a]	Obs.ID	Start	Stop	Exposure	Count Rate[b]	kT_{BB}	R_{BB}	Flux[c]
		YYYY-MM-DD hh:mm:ss (TT)		(ks)	(counts s^{-1})	(keV)	(km)	(10^{-12} cgs)
NICER/XTI	3020560152[d16]	2020-09-19 01:50:25	2020-09-19 02:13:40	1.2	0.30±0.02	0.50±0.04	1.2±0.2	1.3±0.4
Swift/XRT (WT)	00033349088	2020-09-19 21:18:08	2020-09-19 23:07:56	1.5	0.06±0.01	–	–	–
NICER/XTI	3020560153[d16]	2020-09-25 05:05:56	2020-09-25 09:55:17	1.4	0.36±0.02	0.50±0.04	1.2±0.2	1.3±0.4
XMM–Newton/EPIC-pn (FF)	0871191301[f]	2020-10-01 17:22:30	2020-10-02 16:05:13	55.7	0.244±0.002	0.44±0.01	1.6±0.1	1.3±0.1
NuSTAR FPMA/B	80602313008[f]	2020-10-04 06:31:09	2020-10-05 04:51:09	40.6/40.2	0.063±0.002	0.44±0.01	1.6±0.1	1.3±0.1
NICER/XTI	3655010401[d17]	2020-10-06 01:24:13	2020-10-06 23:32:20	9.1	0.46±0.01	0.45±0.01	1.4±0.1	1.7±0.1
NICER/XTI	3655010402[d17]	2020-10-07 00:17:19	2020-10-07 11:27:40	14.6	0.30±0.01	0.45±0.01	1.4±0.1	1.7±0.1
Swift/XRT (PC)	00033349089	2020-10-08 21:26:39	2020-10-08 23:05:37	2.0	0.026±0.003	$0.32^{+0.07}_{-0.06}$	$2.6^{+3.0}_{-0.9}$	$1.2^{+0.4}_{-0.3}$
NICER/XTI	3020560154[d18]	2020-10-09 12:55:44	2020-10-09 22:19:00	0.9	0.37±0.03	0.46±0.02	1.5±0.1	1.0±0.1
Swift/XRT (WT)	00033349090	2020-10-09 22:31:00	2020-10-10 00:19:00	2.5	0.32±0.01	–	–	–
NICER/XTI	3020560155[d18]	2020-10-10 02:50:21	2020-10-10 21:33:20	1.9	0.37±0.02	0.46±0.02	1.5±0.1	1.0±0.1
Swift/XRT (WT)	00033349092	2020-10-11 16:07:14	2020-10-11 18:12:11	3.4	0.045±0.004	–	–	–
Swift/XRT (PC)	00033349093	2020-10-12 03:20:14	2020-10-12 13:07:52	1.8	0.026±0.004	$0.54^{+0.09}_{-0.08}$	$1.0^{+0.5}_{-0.2}$	1.3±0.2
NICER/XTI	3020560157[d18]	2020-10-13 06:47:59	2020-10-13 19:24:51	2.1	0.31±0.02	0.46±0.02	1.5±0.1	1.0±0.1
Swift/XRT (PC)	00033349094	2020-10-13 13:01:52	2020-10-13 20:59:52	1	0.023±0.005	$0.41^{+0.09}_{-0.07}$	$1.7^{+1.5}_{-0.5}$	0.9±0.2
Swift/XRT (PC)	00033349095	2020-10-14 07:46:27	2020-10-14 22:24:52	0.9	0.025±0.005	0.4±0.1	1.4±0.5	$1.4^{+0.8}_{-0.4}$
NICER/XTI	3020560159[d19]	2020-10-16 21:40:00	2020-10-16 23:33:51	1.4	0.41±0.02	0.47±0.01	1.4±0.1	0.9±0.1
NICER/XTI	3020560160[d19]	2020-10-17 00:37:21	2020-10-17 08:36:42	11.1	0.34±0.01	0.47±0.01	1.4±0.1	0.9±0.1
NICER/XTI	3020560161[d19]	2020-10-18 18:13:20	2020-10-18 23:33:00	5.8	0.27±0.01	0.47±0.01	1.4±0.1	0.9±0.1
NICER/XTI	3020560162[d20]	2020-10-19 00:25:24	2020-10-19 22:46:00	13.5	0.37±0.01	0.47±0.01	1.4±0.1	1.2±0.1
NICER/XTI	3020560163[d20]	2020-10-19 23:40:02	2020-10-20 21:59:40	16.8	0.33±0.01	0.47±0.01	1.4±0.1	1.2±0.1
NICER/XTI	3020560164[d21]	2020-10-21 00:27:02	2020-10-21 22:46:00	6.6	0.35±0.01	0.48±0.01	1.3±0.1	1.3±0.1
NICER/XTI	3020560165[d21]	2020-10-21 23:44:35	2020-10-22 20:26:40	4.4	0.38±0.01	0.48±0.01	1.3±0.1	1.3±0.1
NICER/XTI	3020560166[d22]	2020-10-24 13:42:00	2020-10-24 23:22:12	7.4	0.48±0.01	0.44±0.02	1.3±0.1	3.5±0.2
NICER/XTI	3020560167[d22]	2020-10-25 11:20:59	2020-10-25 22:36:29	6.0	0.50±0.01	0.44±0.02	1.3±0.1	3.5±0.2
NICER/XTI	3020560168[d23]	2020-10-25 23:44:58	2020-10-26 23:25:40	8.4	0.46±0.01	0.45±0.02	1.2±0.1	3.3±0.1
NICER/XTI	3020560169[d23]	2020-10-28 12:12:01	2020-10-28 21:45:40	2.3	0.49±0.02	0.45±0.02	1.2±0.1	3.3±0.1
NICER/XTI	3020560170[d24]	2020-11-12 15:06:40	2020-11-12 21:36:12	2.6	0.47±0.01	0.48±0.01	1.3±0.1	0.9±0.1
NICER/XTI	3020560171[d24]	2020-11-13 12:39:00	2020-11-13 22:38:00	6.7	0.33±0.01	0.48±0.01	1.3±0.1	0.9±0.1
NICER/XTI	3020560172[d25]	2020-11-19 11:10:56	2020-11-19 22:26:49	4.4	0.32±0.01	0.44±0.01	1.5±0.1	1.8±0.1
NICER/XTI	3020560173[d25]	2020-11-20 11:55:00	2020-11-20 23:33:00	11.6	0.40±0.01	0.44±0.01	1.5±0.1	1.8±0.1

Radio Instrument	Frequency	Bandwidth	Start	Stop	Exposure	Flux Density Upper Limit[g]	Fluence Upper Limit[g]
	(GHz)	(MHz)	YYYY-MM-DD hh:mm:ss (TT)		(hr)	Periodic Emission (mJy)	Single Pulse (mJy ms)
SRT	1.5	460	2020-10-09 15:51:30	2020-10-09 19:04:12	2 × 1.3	0.1	800
SRT	1.5	460	2020-10-10 16:31:12	2020-10-10 13:49:30	2 × 1.3	0.1	800

[a] The instrumental setup is indicated in brackets: TE = timed exposure, FF = full frame, PC = photon counting, WT = windowed timing.

[b] Count rate, computed after removing bursts, in the 0.3–10 keV range for *Swift* and *XMM–Newton*, in the 0.3–8 keV interval for *Chandra*, in the 1–5 keV band for *NICER*, and in the 3–20 keV range for *NuSTAR* summing up the two FPMs. Uncertainties are at 1σ c.l.

[c] Observed 0.3–10 keV flux in units of 10^{-12} erg cm^{-2} s^{-1}.

[*] These observations were merged in the spectral analysis.

[d,e,f] The spectra extracted from these observations were fitted jointly, tying up all model parameters (see Section 3.2.1 for details).

[g] Upper limits are computed using the radiometer equation (Lorimer & Kramer 2004), assuming a pulse duty cycle of 5%.

ORIGINAL UNEDITED MANUSCRIPT

Downloaded from https://academic.oup.com/mnras/advance-article/doi/10.1093/mnras/stac1314/6584863 by UCL Library Services user on 16 May 2022

2 X-RAY OBSERVATIONS AND DATA REDUCTION

Table 1 reports a log of the X-ray observations of SGR J1935 analysed in this work. These comprise three *Chandra* pointings (two of which unpublished) and one *XMM–Newton* pointing carried out in 2020 between April 30 and May 18 (see also Göğüş et al. 2020), and subsequent multi-instrument observations performed until 2020 November 20. These data sets complement those already presented by Borghese et al. (2020), and provide a total time coverage spanning about 7 months since the source reactivation on 2020 April 27.

Data reduction was performed using tools in the HEASoft package (v. 6.29c), the Science Analysis Software (v. 19) and the *Chandra* Interactive Analysis of Observations (v. 4.12) with the most recent calibration files. We referred photon arrival times to the Solar system barycenter using the *Chandra* position. (R.A. = $19^{\rm h}34^{\rm m}55^{\rm s}.598$, decl. = $+21^\circ53'47''.79$, J2000.0; Israel et al. 2016) and the JPL planetary ephemeris DE 200. In the following, we derive all quantities assuming a distance of 6.6 kpc (Zhou et al. 2020) and all uncertainties are quoted at 1σ confidence level (c.l.).

Diffuse emission, due to a scattering halo around the source, was detected at the outburst onset (Mereghetti et al. 2020). A detailed analysis of this component is beyond the scope of this work and will be presented in a future paper (Tiengo et al., in preparation). To avoid any contamination from the diffuse emission, we selected the background region far from the source (at an angular separation of at least 150 arcsec).

2.1 *Swift*

The *Swift* X-ray Telescope (XRT; Burrows et al. 2005) observed the source 29 times in 2020 between May 28 and October 14, with single exposures ranging from ∼0.5 to ∼3.4 ks. The *Swift*/XRT was configured in photon counting (PC) mode in 21 observations, giving a readout time of about 2.5 s. The remaining observations were performed in windowed timing mode (WT; readout time of 1.8 ms). We reprocessed the data using standard prescriptions[1]. For the PC-mode observations, we extracted source photons from a circle centered on the source with a radius of 20 pixels, and background photons from an annulus with radii of 40 and 80 pixels, free of sources (1 XRT pixel corresponds to about $2''.36$). For the WT-mode observations we collected the source photons from a box of size 20×40 pixels centered on the source, and estimated the background from a region of the same size located far from the source. Net count rates are listed in Table 1. Only the data sets collected in the PC-mode were used for the spectral analysis, whereas the WT-mode data were inspected only for the presence of short bursts.

2.2 *XMM–Newton*

SGR J1935 was observed with the European Photon Imaging Camera (EPIC) on board the *XMM–Newton* satellite on 2020 May 13–14 and October 1–2 for an exposure time of 47.5 ks and 81.5 ks, respectively (for completeness, we included the observation ID 0871190201, already published by Göğüş et al. 2020). In both pointings, the EPIC-pn (Strüder et al. 2001) was operating in Full Frame mode (FF; timing resolution of 73.4 ms). The MOS cameras (Turner et al. 2001) were set in FF mode (timing resolution of 2.6 s) in the first observation and in Small Window mode (SW; timing resolution of 0.3 s) during the second one. Here, we used only the data acquired with the EPIC-pn, which provides the data set with the highest counting statistics owing to its larger effective area compared to the MOS cameras.

Standard analysis procedures were applied in the extraction of the scientific products. We cleaned the observations for periods of high background activity, resulting in a net exposure of 28.3 ks and 55.7 ks for the two observations. We collected the source photons from a circle of radius 30 arcsec. The background level was estimated from a 60-arcsec-radius circle far from the source, on the same CCD. We checked for the potential impact of pile-up through the EPATPLOT tool and found a negligible pile-up fraction of ∼0.3%. The response matrices and ancillary files were generated by means of the RMFGEN and ARFGEN tasks, respectively. Background-subtracted and exposure-corrected light curves were extracted using EPICLCCORR.

2.3 *Chandra*

Three observations of SGR J1935 were carried out by *Chandra* using the Advanced CCD Imaging Spectrometer (ACIS; Garmire et al. 2003) since the onset of the latest outburst in 2020 April for a total on-source exposure time of 88.5 ks. The ACIS was set in timed exposure (TE) mode with a frame readout time of 3.14 s and the source was always positioned on the back-illuminated S3 chip. The timing resolution is too coarse to study the magnetar timing properties, therefore we include these data sets only in the spectral analysis. The observation ID 23251 was already presented by Göğüş et al. (2020). However, we re-analysed it consistently with our approach.

Source photons were selected from a 1.5-arcsec circular region centered on the source, while the background counts were extracted from a circle with a radius of 40 arcsec far from the source. We estimated the impact of pile-up with WebPimms[2] and found that its fraction ranges from 13% to 18% across the different observations. Hence, pile-up is not negligible in our data. We created the source and background spectra, the associated redistribution matrices and ancillary response files using the SPECEXTRACT script, and accounted for the effects of pile-up as explained in Section 3.2.1.

2.4 *NuSTAR*

NuSTAR (Harrison et al. 2013) observed SGR J1935 at two epochs, in 2020 June and in 2020 October. The total on-source exposure times were 70.7 ks and 69.6 ks for the focal plane module A and B (FPMA and FPMB hereafter), respectively. We processed the event lists and filtered out passages of the satellite through the South Atlantic Anomaly using the tool NUPIPELINE. Both source and background counts were accumulated within a circular region of radius 100 arcsec. We then applied the script NUPRODUCTS to extract light curves and spectra, and generate response files for both FPMs. The source was detected up to ∼20 keV in both observations at a net count rate of ∼0.07 counts s^{-1} and ∼0.06 counts s^{-1} in 2020 June and October (summing up the two FPMs), respectively.

2.5 *NICER*

The X-ray Timing Instrument (XTI) of the *NICER* mission (Gendreau et al. 2012) monitored SGR J1935 intensively in 2020, starting from its reactivation on April 27. In this work, we focus on 71 observations, performed between 2020 May and November, for a total on-source exposure time of ∼220 ks. The pointings acquired between

[1] See https://www.swift.ac.uk/analysis/xrt/index.php

[2] https://heasarc.gsfc.nasa.gov/cgi-bin/Tools/w3pimms/w3pimms.pl.

ORIGINAL UNEDITED MANUSCRIPT

Downloaded from https://academic.oup.com/mnras/advance-article/doi/10.1093/mnras/stac1314/6584863 by UCL Library Services user on 16 May 2022

2020 April 28 and July 26 were already presented by Younes et al. (2020). However, we decided to re-analyse them adopting a consistent approach with ours.

We processed the data via the NICERDAS pipeline, using the NICERL2 tool and adopting standard filtering criteria. We created the ancillary response and response matrix files with the tools NICERARF and NICERRMF, respectively. The background count rates and spectra are computed through the NIBACKGEN3C50 tool.

3 X-RAY ANALYSIS AND RESULTS

3.1 Timing Analysis

The arrival times of the *XMM–Newton*/EPIC-pn photons extracted from the source and background regions were corrected to the barycenter of the Solar system. Coherent pulsations were detected in the power spectra of both data sets at a high significance level ($>11\sigma$; Israel & Stella 1996). By means of a phase-fitting timing analysis in each pointing, we inferred the following best period: $P = 3.247361(6)$ s for observation ID 0871190201 (EPIC-pn data only; 2020 May 13) and $P = 3.247778(6)$ s for observation ID 0871191301 (EPIC-pn plus EPIC-MOSs merged data; 2020 October 1). The former period is in agreement, within the uncertainties, with that reported by Göğüş et al. (2020). Figure 1 shows the corresponding light curves folded on the above periods as a function of energy for the two epochs. The pulse profile exhibits a quasi-sinusoidal shape below 1 keV, well-fit by a sine function, and evolves to a more complex morphology with increasing energy, requiring a second sine to properly model the shape and displaying two peaks separated by ∼0.47 in phase in the 5–10 keV range. The pulsed fraction (defined as the semi-amplitude of the fundamental divided by the average count rate) increased from (14±2)% in the 0.3–1 keV interval to (30±2)% in the 5–10 keV interval in 2020 May, while we detected pulsations till 5 keV during the second observation. We set a 3σ upper limit of ∼16% in the 5–10 keV band in 2020 October. Moreover, the broad-band (0.3–10 keV) pulsed fraction dropped from (18±1)% to (10±1)% between the two epochs.

A similar procedure was followed for *NuSTAR* data sets (we selected photons in the 3–12 keV and 3–5 keV ranges) and the pulsar signal was searched in a narrow period interval around the value inferred from the *XMM–Newton* data. No significant signal was detected and 3σ upper limits in the 24%–40% range were obtained for the pulsed fraction.

Based on the above inferred periods and those already reported by Borghese et al. (2020), hence covering a time span of ∼5 months from 2020 April 28 till October 1, we inferred a first period derivative $\dot{P} = 3.5(1)\times10^{-11}$ s s^{-1}. This estimate is a factor 2.5 higher than the period derivative derived during the first four months of the 2014 outburst with a phase-coherent analysis ($\dot{P} \sim 1.4\times10^{-11}$ s s^{-1}; Israel et al. 2016).

3.2 Spectral Analysis

The spectral fitting was performed using XSPEC (Arnaud 1996). We adopted the TBABS model with cross-sections of Verner et al. (1996) and elemental abundances of Wilms et al. (2000) to calculate the effects of the photoelectric absorption along the line of sight. Following our previous work (Borghese et al. 2020), we fixed the hydrogen column density to $N_{\rm H} = 2.3 \times 10^{22}$ cm^{-2}, that is, the value inferred from a systematic analysis of high quality data acquired during the previous outbursts of SGR J1935 (Coti Zelati et al. 2018; see also Younes et al. 2017).

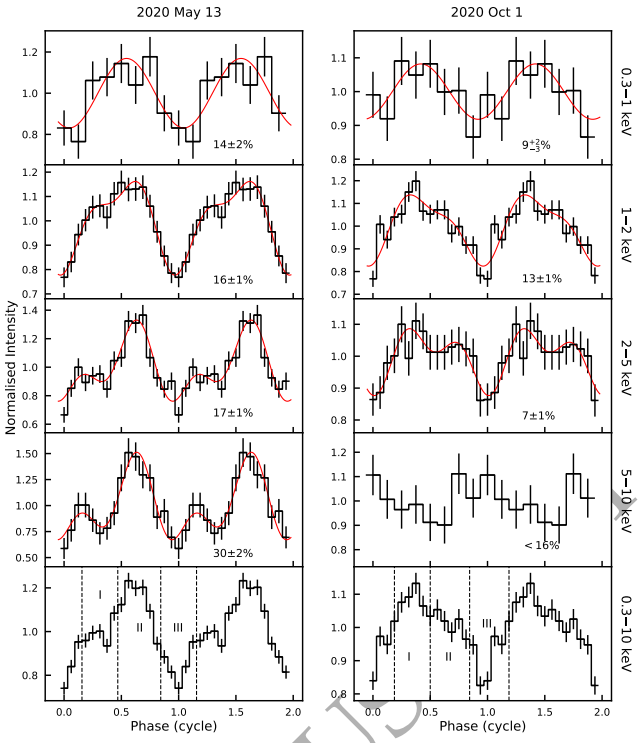

Figure 1. *XMM–Newton* EPIC-pn background-subtracted, energy-resolved pulse profiles for the 2020 May (left-hand panel) and October (right-hand panel) data sets. In the bottom panel, the dashed lines indicate the intervals used in the phase-resolved spectral analysis. Two cycles are shown for clarity.

Due to the low photon counting statistics, the *Swift*/XRT background-subtracted spectra were grouped to have at least five counts in each spectral channel and the W-statistic was employed for model parameter estimation and error calculation. For *NuSTAR*, *XMM–Newton*, *Chandra* and *NICER*, we binned the spectra to guarantee at least 50 background-subtracted counts per energy bin so as to use the χ^2 statistics, unless otherwise specified.

3.2.1 *Phase-averaged spectral analysis*

We fit the *XMM–Newton* and *Swift*/XRT spectra in the 0.5–10 keV energy range, and the *Chandra* and *NICER* ones in the 0.3–8 keV and 1–5 keV intervals, respectively. For the *NuSTAR* pointings, the spectral analysis was limited to the 3–20 keV energy band owing to the very low source signal-to-noise ratio above 20 keV.

We start the fitting procedure by modelling the broadband spectra for the epochs 2020 May 11–13[3], June 14 and October 1–4. For each epoch, we fit the spectra jointly, forcing the model parameters to be the same across the data sets. Moreover, we include a multiplicative normalization which was frozen to one for the *NuSTAR*/FPMA spectrum, and allowed to vary for the other instruments. This term takes into account cross-calibration uncertainties between different instruments. Similarly as in the early stages of the outburst (Borghese et al. 2020), the spectra are well described by an absorbed blackbody

[3] We fit jointly the spectra extracted from the observations *XMM–Newton* ID 0871190201 and *NuSTAR* ID 80602313004. The latter was already presented in our previous work (Borghese et al. 2020).

ORIGINAL UNEDITED MANUSCRIPT

Downloaded from https://academic.oup.com/mnras/advance-article/doi/10.1093/mnras/stac1314/6584863 by UCL Library Services user on 16 May 2022

plus a power-law component (BB+PL; see Figure 2). The best-fitting parameters are listed in Table 2, where we also include the results of the broadband spectral analysis of the observations performed close to the outburst onset (2020 May 2). The 0.3–20 keV luminosity decreased from $(4.0 \pm 0.3) \times 10^{34}\ d_{6.6}^2$ erg s^{-1} on 2020 May 2 to $(2.3 \pm 0.1) \times 10^{34}\ d_{6.6}^2$ erg s^{-1} on Oct 1–4, with a contribution of the power-law component of ∼75% and ∼45% respectively, in the same energy band ($d_{6.6}$ is the source distance in units of 6.6 kpc). We did not detect a clear time evolution of the photon index Γ, which attained a value of ∼1.2, and of the radius of the thermal emitting region, with an average value of $R_{\rm BB}$ ∼1.4 km. On the other hand, the PL normalization decreased by a factor of ∼2.5 and $kT_{\rm BB}$ decreased from $0.59^{+0.06}_{-0.05}$ keV to 0.44±0.01 keV during the time span covered by the broadband observations (2020 May 2 – October 4).

We then fit the same model to the *Swift*/XRT spectra jointly, freezing the $N_{\rm H}$ to the above value. We allowed the other parameters to vary, although the photon index was not constrained over the energy range covered by *Swift*. Hence, we fixed this parameter to Γ=1.2, that is, the averaged value derived from the broadband spectral analysis including *NuSTAR* spectra. The same procedure was applied to the *NICER* spectra. To increase the source signal-to-noise, we fitted together *NICER* spectra extracted from observations performed a few days apart, tying up all model parameters (see Table 1). Given the limited energy interval (1–5 keV), Γ was frozen to 1.2 in this fit as well. We obtained a W-stat = 856.55 for 881 degrees of freedom (d.o.f.) for the *Swift* data and χ^2/ = 3092.3 for 2495 d.o.f. for the *NICER* data sets.

For the *Chandra* spectra, we estimated a pile-up fraction of 13–18%. To correct for this effect, we included the multiplicative pile-up model (Davis 2001), as implemented in XSPEC, in the spectral fitting procedure. Following 'The *Chandra* ABC guide to Pileup'[4], we allowed the grade migration parameter α to vary and fixed the parameter *psffrac* equal to 0.95, that is, we assumed that 95% of events are contained within the central, piled-up portion of the source point spread function. We fit simultaneously the three spectra adopting an absorbed BB+PL model corrected by the pile-up model. As before, we fixed $N_{\rm H}$=2.3 × 10^{22} cm^{-2} and Γ=1.2. The fit yielded χ^2 = 177.83 for 181 d.o.f.

The best-fitting values for the radius and temperature of the blackbody component and the total observed flux (0.3–10 keV) corresponding to each observation are reported in Table 1. Figure 3 shows the temporal evolution of these quantities. After an initial rapid decrease over the course of a few days, the blackbody temperature settled on a steady value of ∼0.45 keV; while the blackbody radius did not show a strong variability, attaining an average value of ∼1.6 km during the ∼200 days covered by the monitoring campaign. These values are consistent with those derived for the BB component during the previous outbursts, when the soft (<10 keV) spectra were described by a BB+PL model and did not show any spectral variability, except for the brightness (Younes et al. 2017). Moreover, they are compatible also with the averaged spectral parameters of the BB component ($kT_{\rm BB}$ ∼ 0.45 keV and $R_{\rm BB}$ ∼ 1.5 km) as obtained from *NICER* observations carried out during 2017–2019 (Younes et al. 2020).

[4] See http://cxc.harvard.edu/ciao/download/doc/pileup_abc.pdf.

3.2.2 *Quiescent level*

The quiescent level of SGR J1935 is still unknown. In our previous work (Borghese et al. 2020), we assumed the value derived from the *Swift*/XRT observation performed 4 days before the outburst onset (ID 00033349044; 2020 April 23). The source signal-to-noise ratio was not high enough to perform a sensitive spectral analysis, therefore we used WEBPIMMS to derive an estimate of the observed flux, ∼4.5×10^{-13} erg cm^{-2} s^{-1} (0.3–10 keV; assuming a BB spectrum with $N_{\rm H}$=2.3×10^{22} cm^{-2} and $kT_{\rm BB}$=0.5 keV). Younes et al. (2020) used the average obtained from the *NICER* 2017–2019 monitoring campaign as a flux reference value (∼6.7×10^{-13} erg cm^{-2} s^{-1} adopting a BB model with $N_{\rm H}$=2.4×10^{22} cm^{-2}, $kT_{\rm BB}$=0.45 keV and unabsorbed flux of 2×10^{-12} erg cm^{-2} s^{-1}; 0.3–10 keV). Finally, Coti Zelati et al. (2018) performed a systematic spectral study of the major magnetar outbursts occurred up to the end of 2016 and identified the quiescent level of SGR J1935 with the flux measured in the *XMM–Newton* observation performed on 2014 October 4, (8.6±0.2)×10^{-13} erg cm^{-2} s^{-1} (0.3–10 keV; 2BB). *XMM–Newton*/EPIC provides the most accurate characterization of the spectrum of SGR J1935 at the faint flux levels observed outside the outburst episodes. Hence, we deem that the last observation provides the most reliable approximation to the true quiescent level for this source. To be consistent with our analysis, we re-fit the *XMM–Newton*/EPIC-pn spectrum with a BB+PL model freezing $N_{\rm H}$=2.3×10^{22} cm^{-2}. The fit gave an overall satisfactory description with $kT_{\rm BB}$ = 0.48±0.01 keV, $R_{\rm BB}$ = 1.1±0.1 km and Γ = $1.9^{+0.5}_{-1.4}$ (χ^2 = 25.8 for 27 d.o.f.). We estimated the quiescent level of the observed flux to be equal to (8.7±0.3)×10^{-13} erg cm^{-2} s^{-1}, that corresponds to a quiescent luminosity of (1.3±0.1)×10^{34} erg s^{-1} (0.3–10 keV).

3.2.3 *Phase-resolved spectroscopy*

We performed a phase-resolved spectral analysis using the two *XMM–Newton*/EPIC-pn data sets, where we detected the source spin period signal with high significance. We extracted spectra from three phase intervals (see Figure 1, bottom panels) and fitted them using an absorbed BB+PL model. Similarly to the phase-averaged spectral analysis, the column density was held fixed at $N_{\rm H}$ = 2.3×10^{22} cm^{-2} for all the fits.

Firstly, for each epoch, we allowed only the normalizations of each component to vary, while the blackbody temperature and photon index were frozen at their best-fitting values for the corresponding phase-averaged spectrum (see Table 2). The fit yielded χ^2 = 206.9 for 159 d.o.f. and χ^2 = 187.9 for 169 d.o.f. for the data sets acquired on 2020 May 13 and October 1, respectively. We obtained statistically equivalent fits by allowing all parameters to vary among the phase-resolved spectra, with χ^2 = 205.1 for 153 d.o.f. (2020 May) and 179.8 for 163 d.o.f. (2020 October). The best-fitting values are listed in Table 3. The blackbody radius and temperature do not show significant variations with the spin phase, while some hints for a phase dependence of the power-law index may be present.

3.3 Burst Search and Spectral Modelling

A search for short X-ray bursts was performed on all available data sets, using the same method outlined by Borghese et al. (2020) (see also, e.g., Gavriil et al. 2004). We extracted the time series with time resolutions of 2.5073 s for the *Swift*/XRT PC-mode data, of 73.36 ms for the *XMM–Newton*/EPIC-pn data sets, and of 1/16, 1/32 and 1/64 s in all other cases. We labelled as bursts the bins with a probability $<10^{-4}(NN_{\rm trials})^{-1}$, where N is the total number of time bins in a

ORIGINAL UNEDITED MANUSCRIPT

Downloaded from https://academic.oup.com/mnras/advance-article/doi/10.1093/mnras/stac1314/6584863 by UCL Library Services user on 16 May 2022

Table 2. Results of the joint spectral fits presented in Section 3.2.

Epoch	kT_{BB} (keV)	R_{BB} (km)	Γ	Norm PL (pho keV^{-1} cm^{-2} s^{-1})	Flux[a] (Obs / Unabs) (10^{-12} erg cm^{-2} s^{-1})	Flux[a] Unabs BB / PL (10^{-12} erg cm^{-2} s^{-1})	χ^2/d.o.f.
2020 May 2[b]	$0.59^{+0.06}_{-0.05}$	$0.85^{+0.35}_{-0.18}$	1.17±0.06	(2.5±0.4)×10^{-4}	5.8±0.1 / 7.8±0.6	2.2±0.5 / 5.6±0.2	148.4/139
2020 May 11–13	0.45±0.01	1.7±0.1	1.24±0.04	(2.5±0.2)×10^{-4}	5.2±0.1 / 7.9±0.2	2.8±0.1 / 5.1±0.1	232.9/232
2020 Jun 14[b]	0.44±0.04	$2.0^{+1.0}_{-0.5}$	1.07±0.11	(9.1±2.1)×10^{-5}	3.4±0.1 / 6.2±0.5	3.7±1.3 / 2.5±0.1	53.17/49
2020 Oct 1–4	0.44±0.01	1.6±0.1	1.23±0.07	(9.9±1.4)×10^{-5}	2.5±0.1 / 4.4±0.2	2.4±0.1 / 1.9±0.1	184.6/152

[a] The fluxes are estimated in the 0.3–20 keV energy range.

[b] For these two epochs, the *NuSTAR* spectrum is fitted together with a *Swift* spectrum taken almost simultaneously. For the latter, the W-stat=7 for 7 d.o.f. for May 2 and W-stat=6.8 for 10 d.o.f. for Jun 14.

Table 3. Results of the phase-resolved spectral analysis presented in Section 3.2.3.

2020 May 13			
Phase	kT_{BB} (keV)	R_{BB} (km)	Γ
I	0.47±0.01	1.6±0.1	$0.9^{+0.2}_{-0.3}$
II	0.45±0.01	1.5±0.1	1.0±0.2
III	0.43±0.02	1.6±0.1	1.4±0.2
2020 Oct 1			
Phase	kT_{BB} (keV)	R_{BB} (km)	Γ
I	0.44±0.01	1.5±0.1	1.2±0.3
II	0.46±0.01	1.4±0.1	0.9±0.3
III	0.43±0.01	1.5±0.1	1.2±0.3

given light curve and N_{trials} corresponds to the number of timing resolutions used in the search. In Table 5, we list the epochs of the bursts referred to the Solar system barycenter and Figure A displays their light curves.

On 2020 October 8–9, SGR J1935 entered a new radio active phase with the detection of multiple radio bursts and, for the first time, of pulsed radio emission at the X-ray spin period (Good & Chime/Frb Collaboration 2020; Zhu et al. 2020). On 2020 October 9, *Swift*/XRT observed the source for 2.5 ks and we detected 24 bursts clustered within about ten minutes, corresponding to a burst rate of ~0.04 burst s^{-1}. Unfortunately, no meaningful spectral analysis could be carried out on the bursts detected using *Swift*/XRT owing to severe pile-up and saturation effects at the measured count rates.

On the other hand, meaningful spectra could be extracted for a couple of bursts detected by *NICER*, that is, those dubbed 3655010201 #2 and 3655010301 #1 in Table 5 (these are actually the events with the largest number of counts among the *NICER* sample; see also Table A1). For these events, the background level was estimated from the persistent emission detected in a close-in-time 10-s chunk of the data sets and the spectra were grouped to contain a minimum of 3 counts per spectral bin, allowing us to use the *W*-statistic. The averaged spectra of these bursts were then fitted with an absorbed power-law model, fixing the column density to $N_H = 2.3 \times 10^{22}$ cm^{-2}. We obtained the following best-fitting parameters: $\Gamma = -1.2 \pm 1.1$ and averaged unabsorbed flux $F_{X,unabs} = 3.3^{+3.2}_{-1.6} \times 10^{-8}$ erg cm^{-2} s^{-1} (0.3–10 keV) for burst 3655010201 #2 (W-stat = 4.90 for 9 d.o.f.); $\Gamma = 2.0 \pm 0.3$ and $F_{X,unabs} = 3.2^{+0.7}_{-0.5} \times 10^{-8}$ erg cm^{-2} s^{-1} (0.3–10 keV) for burst 3655010301 #1 (W-stat = 46.83 for 42 d.o.f.).

No significant bursts were detected in the *XMM–Newton*/EPIC-pn light curves.

4 SIMULTANEOUS RADIO OBSERVATIONS

SGR J1935 was observed with the Sardinia Radio Telescope (SRT; Bolli et al. 2015; Prandoni et al. 2017) at 1.5 GHz in 2020 on October 9 and 10, simultaneously with *NICER*, for two consecutive 1.3-hr sessions each day (see Table 1 for details). Data were recorded with the ATNF digital backend PDFB3[5] in search mode over a bandwidth of 460 MHz split into 1 MHz channels. Total intensity data were 2-bit sampled every 100 μs, except for the first half of the October 10 run, where full Stokes data were recorded every 256 μs (the backend showed signs of overheating and the previous configuration was restored for the second part of the run).

The data were folded (with the software DSPSR; van Straten & Bailes 2011) using the ephemeris obtained from X-ray data and using a dispersion measure DM = 332.8 pc cm^{-3} (Andersen et al. 2020), and blindly searched (with the package PRESTO[6]; Ransom 2011) over a DM range from 300 to 360 pc cm^{-3}. A search spanning ±0.1 ms around the nominal period of the pulsar and the same DM range as the blind search was done on the folded data using PDMP (from the software package PSRCHIVE; Hotan et al. 2004). No persistent radio pulsations were found down to a flux density limit of ~ 0.1 mJy.

A search for single pulses was performed on the data using the SPANDAK pipeline[7] (Gajjar et al. 2018) The pipeline uses RFIFIND from the PRESTO package for high-level radio frequency interference (RFI) excision. The search for bursts/single pulses is conducted through HEIMDALL (Barsdell et al. 2012) to quickly search across a DM range from 0 to 1000 pc cm^{-3}. The de-dispersed time-series were searched for pulses using a matched-filtering technique with a maximum window size of 400 ms. Each candidate found by HEIMDALL at DMs within the range 300–400 pc cm^{-3} was scrutinized against all other candidates for each given observation to validate and identify only the genuine ones. A single candidate not resembling RFI was found at a DM compatible with that of the previously observed bursts (see e.g. Kirsten et al. 2021): DM = 332.42 pc cm^{-3}. The candidate had a signal-to-noise ratio $S/N < 7$. In order to verify the genuineness of this candidate, a 1-s segment of data around the candidate

[5] See http://www.srt.inaf.it/media/uploads/astronomers/dfb.pdf

[6] https://github.com/scottransom/presto

[7] https://github.com/gajjarv/PulsarSearch

ORIGINAL UNEDITED MANUSCRIPT

Downloaded from https://academic.oup.com/mnras/advance-article/doi/10.1093/mnras/stac1314/6584863 by UCL Library Services user on 16 May 2022

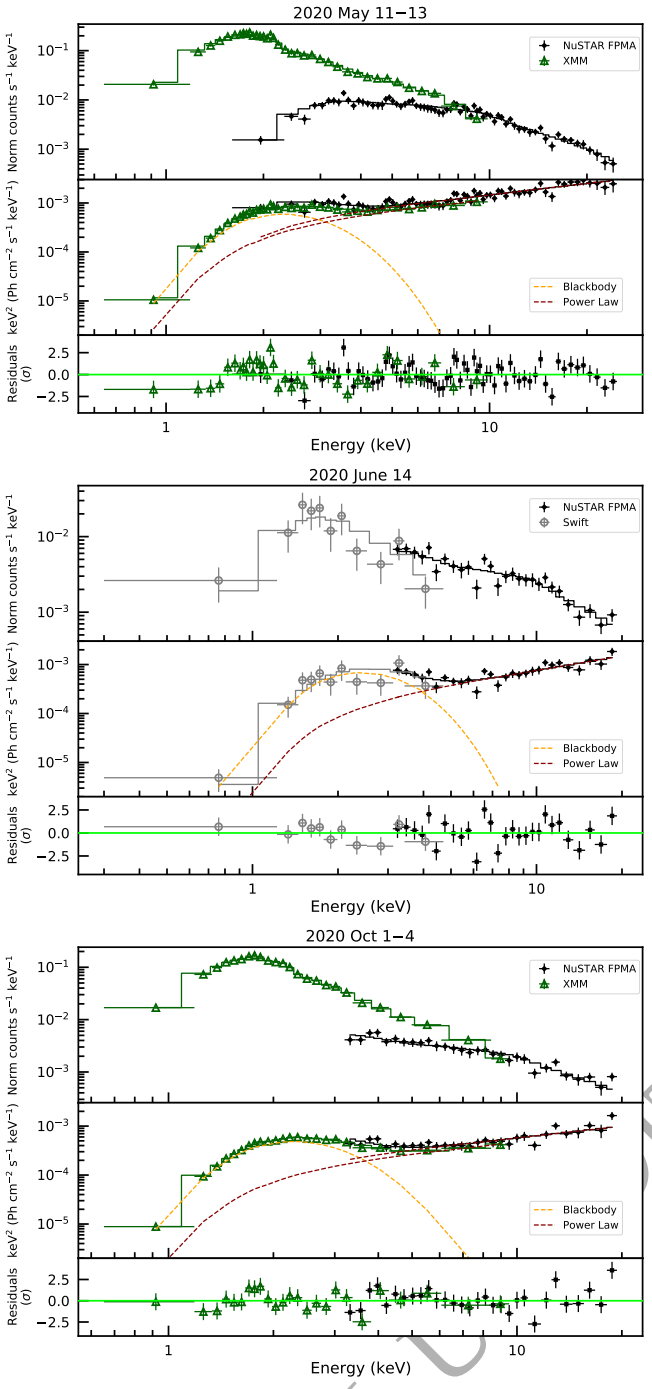

Figure 2. Broadband spectra of SGR J1935 extracted from the quasi-simultaneous *Swift*/XRT (grey), *NuSTAR* (black) and *XMM–Newton* (green) data on 2020 May 11–13 (*top*), June 14 (*middle*), and October 1–4 (*bottom*). *XMM–Newton* data were re-binned for plotting purpose. For each plot, the $E^2 f\,(E)$ unfolded spectrum is shown in the middle panel. Dashed lines mark the contribution of the single components to the spectral model. Post-fit residuals in units of standard deviations are shown in the bottom panel.

has been reprocessed with an ad-hoc program with more sensitive RFI excision procedures taking into account lower level RFI. Firstly, a search for the most corrupted frequency channels in the DM zero data was carried out using the spectral kurtosis algorithm (Nita et al. 2016) as provided by the software package YOUR[8] (Aggarwal et al. 2020). We used a spectral kurtosis thresholding of 5σ. Subsequently, we applied baseline subtraction and the data were normalized for the average bandpass. A check for possible corrupted temporal bins due to the presence of impulsive RFI was then performed with inter-quantile range (IQR) mitigation, similarly to Rajwade et al. (2020). The reprocessed data were then de-dispersed to the derived DM and smoothed via a 2-dimensional Gaussian filter. After this cleaning procedure, the candidate did not display any FRB-like characteristics either in the dynamic spectrum, or in the DM vs time plot, and we concluded that it was originated by RFI corrupted data. With no candidates found, we set an upper limit of 800 mJy on the fluence of a ms-long burst happening during these observations.

Since the data are uncalibrated, all upper limits reported above have been estimated using the modified radiometer equation (see e.g. Lorimer & Kramer 2004) adopting an antenna gain of 0.55 K/Jy, a system temperature of 35 K, a sky temperature of 25 K (accounting also for the supernova remnant hosting SGR J1935), a threshold S/N of 7, and, for the periodic emission, a duty cycle of 5%.

5 DISCUSSION

On 2020 April 27, SGR J1935 entered its fifth recorded outburst phase, placing itself in the short list of magnetars showing recurrent outbursts and frequent bursting activity, including e.g., 1E 1048.1−5937, SGR 1627−41 and CXOU J1647−4552 (An et al. 2018; Borghese et al. 2019; Archibald et al. 2020). This latest outburst stood out from the previous events experienced by SGR J1935 because it was accompanied by a remarkable X-ray burst forest (with more than 200 bursts detected in ∼20 minutes; Younes et al. 2020), and the emission of an intense radio burst with properties resembling those of FRBs and a X-ray counterpart (e.g., Andersen et al. 2020; Mereghetti et al. 2020).

Here we presented the temporal evolution of the spectral and timing properties of the source as tracked by an intensive X-ray monitoring campaign over ∼200 days since the outburst onset, as well as simultaneous radio observations.

5.1 Light curve modelling

To characterise the post-outburst luminosity decay, we modelled the temporal evolution of the 0.3–10 keV luminosity with a phenomenological model consisting of a constant and two exponential functions:

$$L(t) = L_{\rm q} + \sum_{i=1}^{2} A_i \exp(-(t - t_0)/\tau_i)\,, \qquad (1)$$

where $L_{\rm q}$ is the quiescent level, t_0 is the epoch of the outburst onset and the e-folding time τ can be considered as an estimate of the decay timescale. We fixed t_0 to MJD 58966.7683 (2020 April 27, 18:26:20 UTC), that is, the epoch at which *Swift*/BAT triggered on the first burst emitted from SGR J1935 during this latest active period (Barthelmy et al. 2020). For the quiescent luminosity, we assumed the value derived fitting a BB+PL model to the spectrum extracted

[8] https://github.com/thepetabyteproject/your/

ORIGINAL UNEDITED MANUSCRIPT

Downloaded from https://academic.oup.com/mnras/advance-article/doi/10.1093/mnras/stac1314/6584863 by UCL Library Services user on 16 May 2022

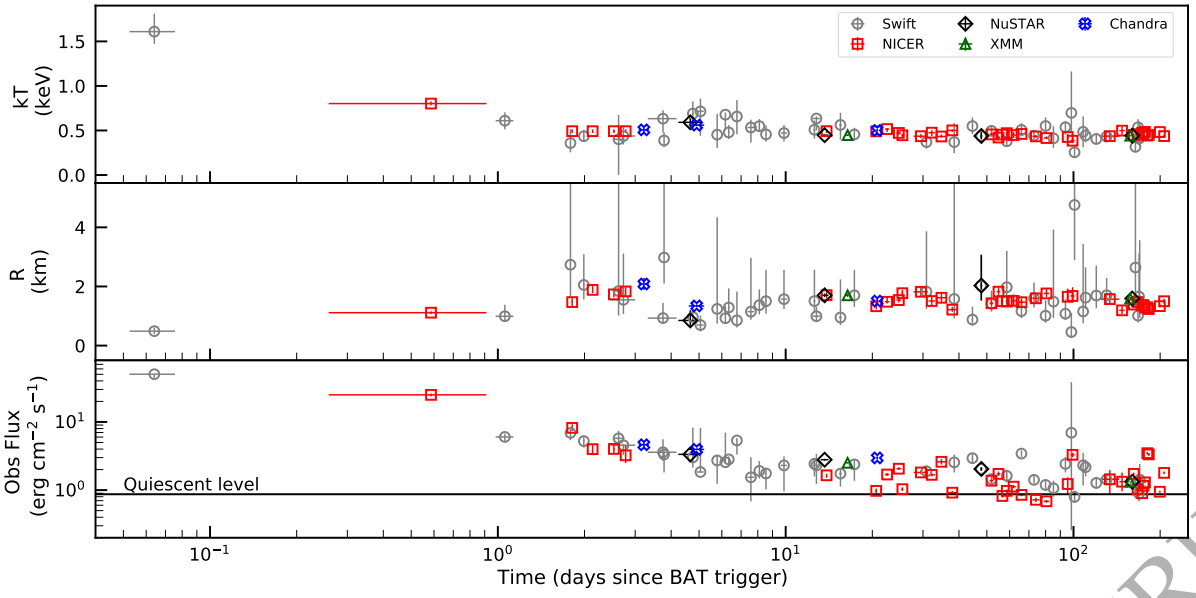

Figure 3. Time evolution of the blackbody temperature (top) and radius (middle) and of the observed flux (bottom) of SGR J1935 between 2020 April 27 and November 20, including observations already presented by Borghese et al. (2020). The observed fluxes are computed in the energy range 0.3–10 keV and are expressed in units of 10^{-12} erg cm^{-2} s^{-1}. The solid line in the bottom panel marks the quiescent flux, $(8.7\pm0.3)\times10^{-13}$ erg cm^{-2} s^{-1}.

from the *XMM–Newton* observation performed on 2014 October 4, $(1.3\pm0.1)\times10^{34}$ erg s^{-1} (see Sec. 3.2.2). A 10 per cent error was assigned to each luminosity. The best-fitting values for the *e*-folding times are τ_1=0.62±0.09 d and τ_2=31.2±3.5 d, highlighting an initial fast decay followed by a slower decrease. The source reached quiescence about ~80 days after the outburst onset, releasing an energy of $\sim5.8\times10^{40}$ erg. Note that the quiescent level of SGR J1935 is not known yet and the true value could be lower than that assumed in this work. Therefore, the released energy and decay timescales should only be considered as a rough estimate. Younes et al. (2020) modelled the flux evolution over a period of three months after the outburst onset. Similar to our results, they found two decay trends described by very different *e*-folding times. The initial rapid decay is characterized by τ_1=0.65±0.08 d, which is consistent with our findings. However, the long-term flux decay has an *e*-folding time of τ_2=75±5 d, which differs from our results. The discrepancy might be due to the different quiescent level we assumed (see Sec. 3.2.2) and/or to the fact that our monitoring campaign extends over a longer period.

Younes et al. (2017) derived the energy emitted for the previous four outbursts within 10 days since the onset (see Table 5 of their paper). The energy released in the first 10 days of the 2020 outburst is equal to $\sim2.6\times10^{40}$ erg, second only to the 2016 June event when the energy was estimated to be $\sim3.6\times10^{40}$ erg. For the first two outbursts in 2014 and 2015, the emitted energy in the first 10 days was $\sim1.2\times10^{40}$ erg, while for the 2016 May episode it was slightly higher, $\sim2\times10^{40}$ erg.

Overall, the values for the decay timescale and the total energy released for the latest outburst of SGR J1935 fall at the low end of the range of values measured for magnetar outbursts. As a matter of fact, the decay time scale of ~30 d is among the shortest τ measured so far. Yet, they are still compatible with the trend of the correlation measured previously, according to which the shorter the outburst, the less energetic. These results imply that the decay pattern of this outburst is not dissimilar from those observed in other magnetars (Coti Zelati et al. 2018).

Table 4. Results of the broadband spectral fitting adopting the NTZ model (see Sec. 5.2).

Epoch	kT (keV)	$\beta_{\rm bulk}$	$\Delta\phi$ (rad)	Norm
May 2	0.67±0.05	0.61±0.04	0.49±0.01	0.026±0.002
May 11	0.48±0.01	0.65±0.02	0.452±0.002	0.034±0.001
Jun14	0.50±0.03	0.72±0.06	0.43±0.01	0.030±0.005
Oct 1	0.48±0.01	0.71±0.04	0.423±0.002	0.024±0.001

5.2 Spectral evolution

About five days after its reactivation, SGR J1935 was observed with *NuSTAR* and *Swift*, revealing a hardening of the spectrum with the appearance of a non-thermal component extending up to ~25 keV. In the following months, three additional broadband observations were performed and still detected hard X-ray emission till ~20 keV. At each epoch, the non-thermal component was well modeled by a PL with a photon index of Γ ~1.2. Its contribution to the total 0.3–20 keV luminosity decreased from ~75% at the outburst peak to ~45% after ~5 months (Table 2). During the whole monitoring campaign, besides the PL component, a blackbody was required to properly model the spectrum. Its temperature rapidly decayed during the first day of the outburst from ~1.5 keV to ~0.6 keV and decreased only slightly down to ~0.45 keV over the following months. The corresponding emitting area was rather steady in time, with a radius of ~1.6 km (Figure 3).

The spectral hardening and the detection of a power law at hard X-rays are ubiquitous properties of magnetars in outburst. The decomposition of the spectral model as a blackbody plus a power-law component is generally interpreted in terms of thermal emission from the cooling neutron star surface that gets affected by physical mechanisms taking place in the magnetosphere, such as Resonant Cyclotron Scattering (RCS; see e.g., Nobili et al. 2008a). The thermal photons

ORIGINAL UNEDITED MANUSCRIPT

Downloaded from https://academic.oup.com/mnras/advance-article/doi/10.1093/mnras/stac1314/6584863 by UCL Library Services user on 16 May 2022

produced at the surface gain energy via repeated scatterings onto charged particles flowing along the magnetic field lines, leading to the formation of a tail at higher energies. During an outburst, magnetic stresses and instabilities induce crustal displacements that can implant a strong twist of the magnetic field lines. The detection of a hot spot suggests that the magnetic twist is localized to a restricted portion of the magnetosphere, most likely to a current-carrying bundle of field lines (Beloborodov 2009).

However, explaining the spectral evolution of SGR J1935 along the outburst within the RCS scenario poses some challenges. In fact, while the blackbody temperature quickly drops as expected (Beloborodov 2009; Pons & Rea 2012), the blackbody radius undergoes little changes and, even more strikingly, the power-law index remains almost constant. Actually, as recent 3D simulations have shown, the heated region can indeed cool without much shrinking (De Grandis et al. 2021) but the power-law should become softer as the twist subsides (Beloborodov 2009). To investigate this further, we fitted the spectra with the NTZ model (Nobili et al. 2008a,b), which accounts for resonant cyclotron up-scattering of the soft seed photons (see Table 4). Taken at face value, the results of the NTZ spectral fits seem to indicate that, while the luminosity of the source is decaying, the decrease in the twist angle $\Delta\phi$ is accompanied by an increase in the velocity $\beta_{\rm bulk}$ of the magnetospheric charges. Since both these quantities control the efficiency of the scattering process and hence the steepness of the power-law tail, this may in turn result in a nearly constant power-law index. The decrease in flux of the non-thermal component may reflect the fact that a smaller fraction of the photons from the thermal emitting area is intercepted by the currents in the bundle.

5.3 Timing properties and pulse profile simulations

Regarding the timing properties, we detected the spin period signal in the two *XMM–Newton* data sets (2020 May 13 and October 1). The pulse profile displays a variable morphology with energy. In the 5–10 keV interval, the profile exhibits a double-peaked shape, as observed in the previous *NuSTAR* observations performed close to the outburst onset (Borghese et al. 2020); while it evolves to a nearly sinusoidal shape at lower energies. The broadband pulsed fraction decreased by a factor of ∼2 between the two epochs. These behaviours are at odds with that observed during the first months of the 2014 outburst, when the pulse profile attained a quasi-sinusoidal shape, with no variation in time and energy, and the broadband pulsed fraction was in the 17–21 % range. These differences may suggest that distinct regions on the neutron star surface are heated during each outburst. By combining the two *XMM–Newton* spin period measurements with those presented by Borghese et al. (2020) (P = 3.24731(1) s on 2020 April 29–30, 3.247331(3) s on May 2 and 3.24731(1) s on May 11), we inferred a long-term average spin-down rate equal to $\dot{P} = 3.5(1)\times10^{-11}$ s s^{-1}, that is a factor 2.5 larger than the $\dot{P}$ measured in 2014 ($\dot{P}$=1.43(1)$\times10^{-11}$ s s^{-1}; Israel et al. 2016). Changes in the pulse profile morphology and in the timing parameters are common during magnetar outbursts, mirroring the magnetosphere variations that follow flaring activity (for a more detailed discussion about the timing behavior of SGR J1935 during 2020 October 1 and November 27 see Younes et al., to be subm.).

Pulsations below 1 keV were detected in both *XMM–Newton* pointings with a pulsed fraction of ∼ 14% on 2020 May 13 and ∼ 9% on October 1 (this value is however compatible with zero at the 3σ level; Figure 1), and the unabsorbed BB flux decreased of about 20% between the two epochs (Table 2). The low measured pulsed fraction is consistent with the (nearly) constant values of the BB parameters over the pulse phase, as derived from the phase-resolved spectroscopy (Section 3.2.3 and Table 3). To gain some insight on the source geometry and on its evolution over the outburst decay, we introduce a simple model according to which thermal photons are produced by a circular cap on the star surface heated at the outburst onset. We assume that the cap is at uniform temperature, as suggested by the lack of multiple BB components in the observed spectrum (this is at variance with, e.g., the case of XTE J1810−197, Borghese et al. 2021). The cap properties are fixed by the measured blackbody temperature ($kT_{\rm c}$ = 0.45 keV) and radius ($R_{\rm BB}$ = 1.6 km which results in a semi-aperture $\theta_{\rm c} \sim 7^\circ$ for $R_{\rm NS}$ = 13 km); these values are representative of both the *XMM–Newton* observations of 2020 May 13 and October 1 since they do not change significantly between the two epochs. We computed the pulse profiles of the thermal component, as seen by an observer at infinity, as a function of the two geometrical angles χ and ξ which measure the inclination of the line-of-sight (LOS) and of the cap axis with respect to the rotation axis, respectively. General-relativistic effects are taken into account (see Turolla & Nobili 2013, for details)[9]. Results for the pulsed fraction are shown in Figure 5.3 where the green/white, labeled contour marks the value of the pulsed fraction derived in the XMM observation ID 0871190201 (2020 May 13) and ID 0871191301 (2020 Oct 1), 14% and 9% respectively; the dashed contours are drawn in correspondence to 1σ errors. Results are not particularly constraining for the source geometry. However, we note that despite the fact that no significant changes in the emission properties of the hot spot were detected, the two values of the PF do not appear to be consistent, at least within 1σ uncertainties. While this can simply reflect measurement errors, taken face value it may suggest that the hot spot (slightly) changed its position on the surface without sensible variations in size and temperature.

During the X-ray monitoring campaign, the SRT observed SGR J1935 twice, on 2020 October 9 and 10, after the detection of three additional radio bursts by CHIME on October 8 (Good & Chime/Frb Collaboration 2020). Moreover, on October 9, the FAST telescope detected multiple radio pulses with fluence up to 40 mJy ms and pulsed radio emission at a period of ∼3.24 s. During the SRT observations, we did not detect either pulsed emission or radio bursts, setting an upper limit on the flux density for the former of 0.1 mJy and on the fluence for the latter of 800 mJy ms. Furthermore, a dedicated multi-frequency campaign was initiated with multiple radio facilities after the 2020 April FRB-like radio burst (Bailes et al. 2021) without any successful detections. This phenomenology indicates that SGR J1935 can swing between a radio-loud and a radio-quiet states, although the connection with the X-ray activity currently remains not well understood and will need to be investigated with more coordinated radio and X-ray observations.

6 ACKNOWLEDGMENTS

AB thanks George Younes for useful discussions and suggestions. We thank the referee, T. Güver, for his helpful comments. This research is based on observations with *Chandra* (NASA), *NICER* (NASA), *NuSTAR* (CaltTech/NASA/JPL), *Swift* (NASA/ASI/UK), *XMM–Newton* (ESA/NASA) and the Sardinia Radio Telescope (SRT). We thank N. Schartel for approving a Target of Opportunity observation with

[9] Interstellar absorption and the detector response function were not accounted for. However, for the particular case we are dealing with (a constant temperature blackbody which changes in phase because of the varying visible area), the pulse profile is independent on both effects and the pulsed fraction is independent on the blackbody temperature.

ORIGINAL UNEDITED MANUSCRIPT

Downloaded from https://academic.oup.com/mnras/advance-article/doi/10.1093/mnras/stac1314/6584863 by UCL Library Services user on 16 May 2022

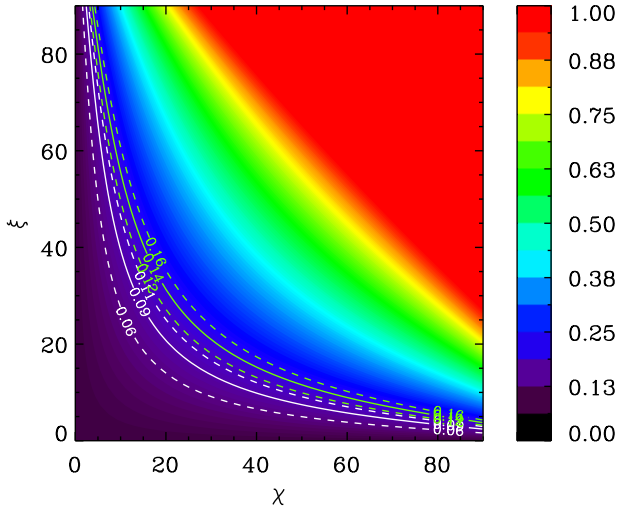

Figure 4. The computed pulsed fraction as a function of the two geometrical angles χ and ξ. The white and green contours correspond to the observed PF for the 2020 October 1 (9%) and of the 2020 May 13 (14%) observation, respectively, together with the associated 1 σ errors (dashed lines); see text for details.

XMM–Newton in the Director's Discretionary Time, and the *XMM–Newton* SOC for carrying out the observation. We also thank the *NICER*, *NuSTAR* and *Swift* teams for promptly scheduling our observations as well as the CHIME/FRB collaboration and the *NICER* team for asking part of the observations presented in this work. The SRT is funded by the Department of University and Research (MIUR), ASI, and the Autonomous Region of Sardinia (RAS) and is operated as National Facility by the National Institute for Astrophysics (INAF). A.B. and F.C.Z. are supported by Juan de la Cierva fellowships. A.B., F.C.Z., and N.R. are supported by grants SGR2017-1383, PGC2018-095512-BI00, and the ERC Consolidator grant "MAGNESIA" (No. 817661). G.L.I., S.M., R.T. and A.T. acknowledge financial support from the Italian MUR through grant PRIN 2017LJ39LM, "UNIAM". G.L.I. also acknowledges funding from ASI-INAF agreements I/037/12/0 and 2017-14-H.O. This work was partially supported by the program Unidad de Excelencia María de Maeztu CEX2020-001058-M. We also acknowledge support from the PHAROS COST Action (CA16214). This research has made use of the following software: CIAO (v4.12; Fruscione et al. 2006, MARX (v5.5.1), SAS (v19; Gabriel et al. 2004), HEASoft (v6.28), FTOOLS (v6.28; Blackburn 1995), XSPEC (v12.11.0h; Arnaud 1996), NICERDAS (v7a), NuSTARDAS (v2.0.0), MATPLOTLIB (v3.2.1; Hunter 2007), NUMPY (v1.18.4; Harris et al. 2020).

7 DATA AVAILABILITY

Radio data can be provided by the authors upon reasonable request. Data from *NICER*, *Swift*, *XMM–Newton*, *Chandra* and *NuSTAR* observations are publicly available.

REFERENCES

Aggarwal K., et al., 2020, Journal of Open Source Software, 5, 2750
An H., Cumming A., Kaspi V. M., 2018, ApJ, 859, 16
Andersen B. C., et al., 2020, Nature, 587, 54
Archibald R. F., Scholz P., Kaspi V. M., Tendulkar S. P., Beardmore A. P., 2020, ApJ, 889, 160
Arnaud K. A., 1996, in Jacoby G. H., Barnes J., eds, Astronomical Data Analysis Software and Systems V Vol. 101, XSPEC: The First Ten Years. ASP, San Francisco, pp 17–20
Bailes M., et al., 2021, MNRAS, 503, 5367
Barsdell B. R., Bailes M., Barnes D. G., Fluke C. J., 2012, MNRAS, 422, 379
Barthelmy S. D., et al., 2020, GRB Coordinates Network, 27657, 1
Beloborodov A. M., 2009, ApJ, 703, 1044
Beloborodov A. M., 2017, ApJ, 843, L26
Bera A., Chengalur J. N., 2019, MNRAS, 490, L12
Blackburn J. K., 1995, in Shaw R. A., Payne H. E., Hayes J. J. E., eds, Astronomical Data Analysis Software and Systems IV. Vol. 77, FTOOLS: A FITS Data Processing and Analysis Software Package. ASP Conf. Ser., San Francisco, CA, p. 367
Bochenek C. D., Ravi V., Belov K. V., Hallinan G., Kocz J., Kulkarni S. R., McKenna D. L., 2020, Nature, 587, 59
Bolli P., et al., 2015, Journal of Astronomical Instrumentation, 4, 1550008
Borghese A., et al., 2019, MNRAS, 484, 2931
Borghese A., Coti Zelati F., Rea N., Esposito P., Israel G. L., Mereghetti S., Tiengo A., 2020, ApJ, 902, L2
Borghese A., et al., 2021, MNRAS, 504, 5244
Burrows D. N., et al., 2005, Space Science Reviews, 120, 165
Caleb M., Keane E., 2021, Universe, 7, 453
Caleb M., et al., 2022, MNRAS, 510, 1996
Coti Zelati F., Rea N., Pons J. A., Campana S., Esposito P., 2018, MNRAS, 474, 961
Davis J. E., 2001, ApJ, 562, 575
De Grandis D., Taverna R., Turolla R., Gnarini A., Popov S. B., Zane S., Wood T. S., 2021, ApJ, 914, 118
Esposito P., Rea N., Israel G. L., 2021, Magnetars: A Short Review and Some Sparse Considerations. Springer Berlin Heidelberg, Berlin, Heidelberg, pp 97–142, doi:10.1007/978-3-662-62110-3_3, https://doi.org/10.1007/978-3-662-62110-3_3
Fruscione A., et al., 2006, in Silva D. R., Doxsey R. E., eds, SPIE Conference Series Vol. 6270, Observatory Operations: Strategies, Processes, and Systems. SPIE, Bellingham, p. 62701V, doi:10.1117/12.671760
Gabriel C., et al., 2004, in Ochsenbein F., Allen M. G., Egret D., eds, Astronomical Data Analysis Software and Systems (ADASS) XIII Vol. 314, The XMM-Newton SAS - Distributed Development and Maintenance of a Large Science Analysis System: A Critical Analysis. San Francisco, CA: ASP, p. 759
Gajjar V., et al., 2018, ApJ, 863, 2
Garmire G. P., Bautz M. W., Ford P. G., Nousek J. A., Ricker Jr. G. R., 2003, in Truemper J. E., Tananbaum H. D., eds, Proceedings of the SPIE. Vol. 4851, X-Ray and Gamma-Ray Telescopes and Instruments for Astronomy.. SPIE, Bellingham, pp 28–44, doi:10.1117/12.461599
Gavriil F. P., Kaspi V. M., Woods P. M., 2004, ApJ, 607, 959
Gendreau K. C., Arzoumanian Z., Okajima T., 2012, in Proc. SPIE. p. 844313, doi:10.1117/12.926396
Good D., Chime/Frb Collaboration 2020, The Astronomer's Telegram, 14074, 1
Göğüş E., et al., 2020, ApJ, 905, L31
Harris C. R., et al., 2020, Nature, 585, 357
Harrison F. A., et al., 2013, ApJ, 770, 103
Hotan A. W., van Straten W., Manchester R. N., 2004, Publ. Astron. Soc. Australia, 21, 302
Hunter J. D., 2007, Computing in Science & Engineering, 9, 90
Israel G. L., Stella L., 1996, ApJ, 468, 369
Israel G. L., et al., 2016, MNRAS, 457, 3448
Israel G. L., et al., 2021, ApJ, 907, 7
Kaspi V. M., Beloborodov A. M., 2017, ARA&A, 55, 261
Kirsten F., Snelders M. P., Jenkins M., Nimmo K., van den Eijnden J., Hessels J. W. T., Gawroński M. P., Yang J., 2020, Nature Astronomy,
Kirsten F., Snelders M. P., Jenkins M., Nimmo K., van den Eijnden J., Hessels J. W. T., Gawroński M. P., Yang J., 2021, Nature Astronomy, 5, 414
Lin L., et al., 2020a, Nature, 587, 63

ORIGINAL UNEDITED MANUSCRIPT

Downloaded from https://academic.oup.com/mnras/advance-article/doi/10.1093/mnras/stac1314/6584863 by UCL Library Services user on 16 May 2022

Lin L., Göğüş E., Roberts O. J., Baring M. G., Kouveliotou C., Kaneko Y., van der Horst A. J., Younes G., 2020b, ApJ, 902, L43
Lorimer D. R., Kramer M., 2004, Handbook of Pulsar Astronomy. Cambridge, UK: Cambridge University Press
Marcote B., et al., 2020, Nature, 577, 190
Margalit B., Beniamini P., Sridhar N., Metzger B. D., 2020, ApJ, 899, L27
Mereghetti S., et al., 2020, ApJ, 898, L29
Nita G. M., Gary D. E., Hellbourg G., 2016, in 2016 Radio Frequency Interference (RFI). pp 75–80, doi:10.1109/RFINT.2016.7833535
Nobili L., Turolla R., Zane S., 2008a, MNRAS, 386, 1527
Nobili L., Turolla R., Zane S., 2008b, MNRAS, 389, 989
Palmer D., 2020, The Astronomer's Telegram, 14208, 1
Pons J. A., Rea N., 2012, ApJ, 750, L6
Prandoni I., et al., 2017, A&A, 608, A40
Rajwade K., et al., 2020, in Evans C. J., Bryant J. J., Motohara K., eds, Vol. 11447, Ground-based and Airborne Instrumentation for Astronomy VIII. SPIE, pp 78 – 85, doi:10.1117/12.2559937, https://doi.org/10.1117/12.2559937
Ransom S., 2011, PRESTO: PulsaR Exploration and Search TOolkit (ascl:1107.017)
Ridnaia A., et al., 2021, Nature Astronomy,
Stamatikos M., Malesani D., Page K. L., Sakamoto T., 2014, GRB Coordinates Network, 16520, 1
Strüder L., et al., 2001, A&A, 365, L18
Tavani M., et al., 2021, Nature Astronomy,
Turner M. J. L., et al., 2001, A&A, 365, L27
Turolla R., Nobili L., 2013, ApJ, 768, 147
Verner D. A., Ferland G. J., Korista K. T., Yakovlev D. G., 1996, ApJ, 465, 487
Wilms J., Allen A., McCray R., 2000, ApJ, 542, 914
Younes G., et al., 2017, ApJ, 847, 85
Younes G., et al., 2020, ApJ, 904, L21
Zhang C. F., et al., 2020, The Astronomer's Telegram, 13699, 1
Zhou P., Zhou X., Chen Y., Wang J.-S., Vink J., Wang Y., 2020, arXiv e-prints, p. arXiv:2005.03517
Zhu W., et al., 2020, The Astronomer's Telegram, 14084, 1
van Straten W., Bailes M., 2011, Publ. Astron. Soc. Australia, 28, 1

APPENDIX A: *NICER* BURSTS: FLUENCE AND DURATION

In Table A1, we list the fluence and durations for the bursts detected in the *NICER*/XTI light curves. Owing to uncertainties related to the detector saturation limits, we do not report these quantities for the bursts identified in the *Swift*/XRT data sets.

In the table, the fluence refers to the 0.3–10 keV range and the duration has to be considered as an approximate value. We estimated it by summing the 15.625-ms time bins showing enhanced emission for the structured bursts, and by setting it equal to the coarser time resolution at which the burst is detected in all the other cases.

Table 5. Log of X-ray bursts detected in the *NICER*/XTI and *Swift*/XRT data sets.

Instrument	Obs.ID[a]	Burst epoch YYYY-MM-DD hh:mm:ss (TDB)
NICER/XTI	3655010201 #1	2020-05-18 07:19:55
	#2	13:39:39
NICER/XTI	3020560106 #1	2020-05-20 14:06:36
NICER/XTI	3020560108 #1	2020-05-23 01:52:53
	#2	05:01:59
NICER/XTI	3655010301 #1	2020-06-17 22:02:05
NICER/XTI	3655010302 #1	2020-06-18 13:20:40
Swift/XRT (WT)	00033349076 #1	2020-07-24 00:21:13
	#2	01:42:58
	#3	01:48:38
Swift/XRT (WT)	00033349084 #1	2020-09-10 23:56:02
	#2	23:59:28
	#3	00:04:29
Swift/XRT (WT)	00033349085 #1	2020-09-11 09:57:07
	#2	10:03:43
	#3	11:18:33
Swift/XRT (WT)	00033349086 #1	2020-09-17 17:13:47
	#2	18:51:31
	#3	18:55:54
Swift/XRT (WT)	00033349087 #1	2020-09-18 00:59:54
	#2	01:03:55
	#3	02:36:07
Swift/XRT (WT)	00033349088 #1	2020-09-19 21:25:43
	#2	22:59:11
	#3	23:09:29
	#4	23:11:05
Swift/XRT (WT)	00033349090 #1	2020-10-09 22:43:38
	#2	22:43:47
	#3	22:44:30
	#4	22:44:55
	#5	22:45:51
	#6	22:46:13
	#7	22:47:29
	#8	22:47:43
	#9	22:47:58
	#10	22:48:08
	#11	22:48:19
	#12	22:48:24
	#13	22:48:31
	#14	22:49:16
	#15	22:50:10
	#16	22:50:12
	#17	22:50:17
	#18	22:50:46
	#19	22:50:47
	#20	22:51:29
	#21	22:52:03
	#22	22:52:43
	#23	22:53:39
	#24	22:53:44
Swift/XRT (WT)	00033349092 #1	2020-10-11 17:53:53
	#2	18:04:27

[a] The notation #N corresponds to the burst number in a given observation.

ORIGINAL UNEDITED MANUSCRIPT

Downloaded from https://academic.oup.com/mnras/advance-article/doi/10.1093/mnras/stac1314/6584863 by UCL Library Services user on 16 May 2022

Table A1. Log of X-ray bursts detected in the *NICER*/XTI light curves.

Obs.ID	Burst epoch YYYY-MM-DD hh:mm:ss (TDB)	Fluence (counts)	Duration (ms)
3655010201 #1	2020-05-18 07:19:55	11	62.5
#2	13:39:39	15	62.5
3020560106 #1	2020-05-20 14:06:36	7	62.5
3020560108 #1	2020-05-23 01:52:53	6	31.25
#2	05:01:59	7	62.5
3655010301 #1	2020-06-17 22:02:05	47	62.5
3655010302 #1	2020-06-18 13:20:40	6	62.5

ORIGINAL UNEDITED MANUSCRIPT

Downloaded from https://academic.oup.com/mnras/advance-article/doi/10.1093/mnras/stac1314/6584863 by UCL Library Services user on 16 May 2022

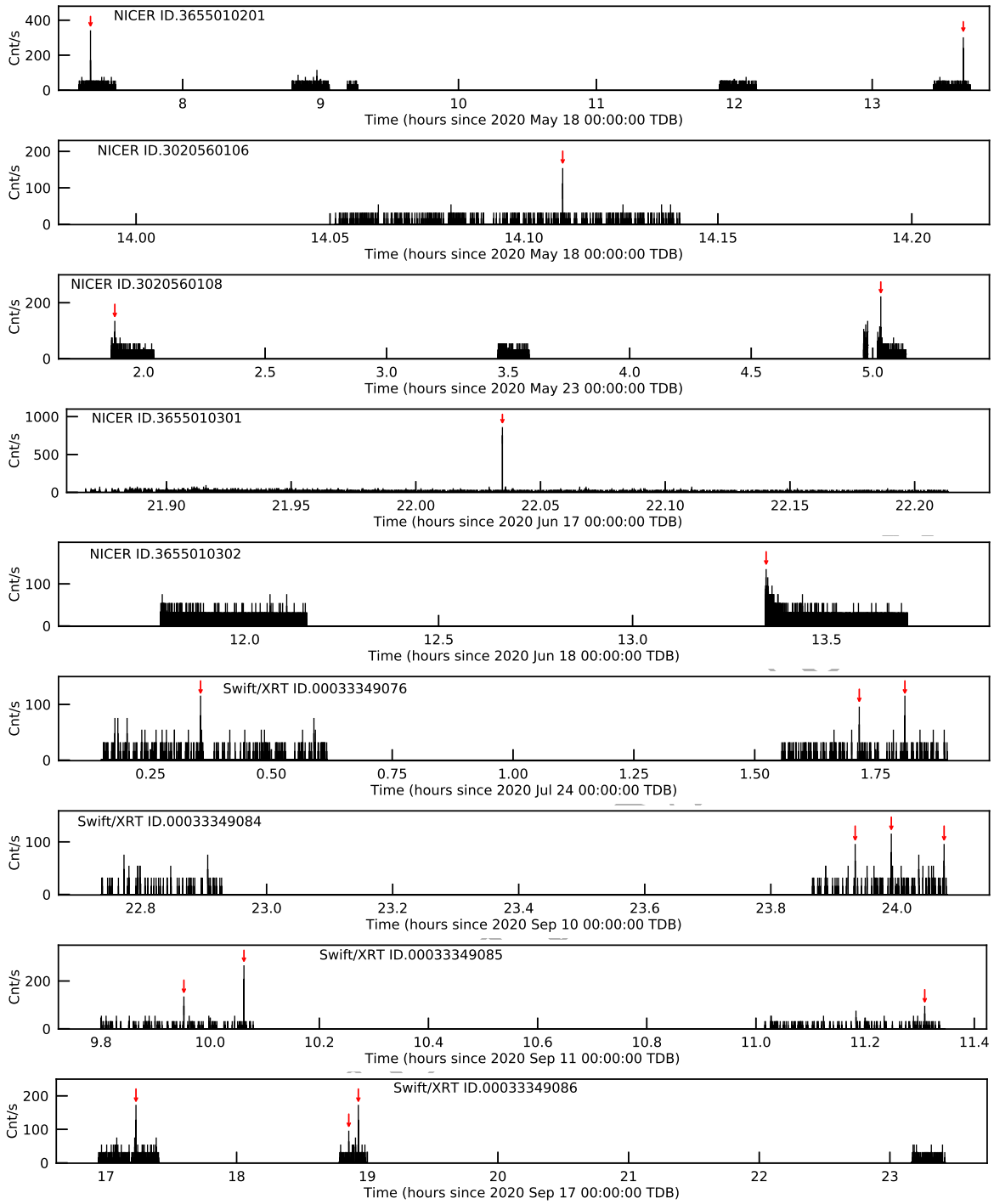

Figure A1. Light curves of SGR J1935 extracted from the *Swift*/XRT (0.3–10 keV), *XMM–Newton* (0.3–10 keV) and *NICER* (0.3–10 keV) data in which we detected bursts. All bursts are marked by arrows. The light curves were binned at 62.5 ms in all cases, except for the *XMM–Newton* data sets where we use a time bin of 73.36 ms.

ORIGINAL

Downloaded from https://academic.oup.com/mnras/advance-article/doi/10.1093/mnras/stac1314/6584863 by UCL Library Services user on 16 May 2022

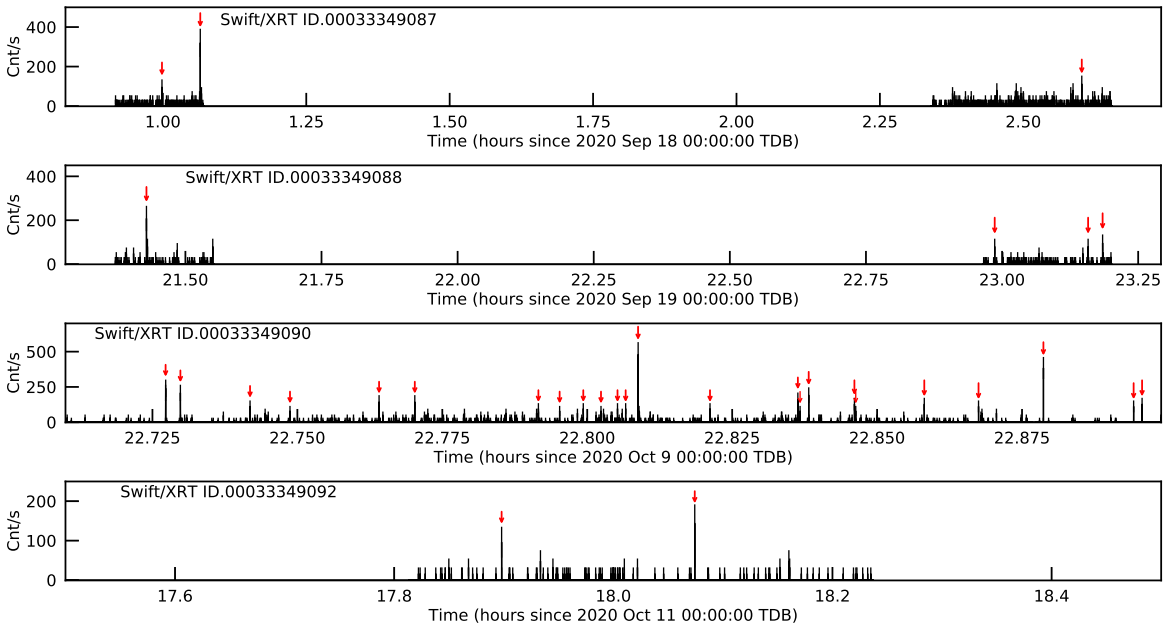

Figure A1 – *continued*

ORIGINAL UNEDITED MANUSCRIPT

Downloaded from https://academic.oup.com/mnras/advance-article/doi/10.1093/mnras/stac1314/6584863 by UCL Library Services user on 16 May 2022